MPC-based postural control

Mimicking CNS strategies for head–neck stabilization under eyes closed conditions

Messiou, Chrysovalanto; Happee, Riender; Papaioannou, Georgios

DOI
10.1016/j.conengprac.2025.106428

Publication date
2025

Document Version
Final published version

Published in
Control Engineering Practice

Control Engineering Practice 164 (2025) 106428

Contents lists available at ScienceDirect

Control Engineering Practice

journal homepage: www.elsevier.com/locate/conengprac

MPC-based postural control: Mimicking CNS strategies for head–neck stabilization under eyes closed conditions

Chrysovalanto Messiou *, Riender Happee, Georgios Papaioannou

Department of Cognitive Robotics, Delft University of Technology, The Netherlands

ARTICLE INFO

Keywords:
Human body modeling
MPC
Compensatory postural adjustments
Central nervous system
Automated vehicle

ABSTRACT

A plausible explanation about the acquisition and realization of beliefs by the central nervous system (CNS) when issuing control actions to counteract external perturbations, is to employ mechanisms aiming to minimize sensory conflict and muscle effort while maintaining biomechanical stability. However, existing head–neck postural control models fail to explicitly integrate this plausible CNS objective within their stabilization mechanisms. This study proposes a novel Model Predictive Control (MPC)-based framework to replicate CNS postural stabilization by incorporating the minimization of sensory conflict as a primary control objective through the MPC cost function. The MPC is integrated in a simplified biomechanical head–neck structure, using a prediction model and sensory feedback to optimize control actions over a finite time horizon within biomechanical constraints. Two human experiments measuring head motion with unpredictable seat and trunk perturbations were used to evaluate and validate different configurations of sensory feedback pathways. During anterior–posterior translational trunk perturbations, the results illustrated that the configuration with vestibular feedback improved head position prediction while muscle effort and partial somatosensory feedback alone, achieved superior results in head pitch prediction. Meanwhile, muscle effort and partial somatosensory feedback were sufficient to stabilize the head during trunk rotational (pitch) perturbations. Finally, a multi-scenario optimization demonstrated that a single set of MPC weights could generalize stabilization across both perturbation types. The results demonstrate the effectiveness of MPC in replicating CNS-inspired postural adjustments, indicating that controlling a simplified biomechanical head–neck model provides a computationally efficient and accurate alternative to complex multi-segment approaches.

1. Introduction

Maintaining balance and orientation is a complex task, particularly in dynamic environments such as moving vehicles. This challenge becomes even more critical in automated vehicles (AV), where unpredictable maneuvers can affect the accuracy of self-motion perception used by the central nervous system (CNS) to restore balance. The CNS plays a crucial role in postural control while being driven. It relies on sensory integration (visual, vestibular and somatosensory), internal models of body and sensory dynamics (Wada, 2021), and adaptive mechanisms, to produce coordinated motor responses that ensure stability and orientation awareness (Forbes et al., 2013). However, the CNS's inference and beliefs for the control process of these motor responses are not yet proven, and only plausible explanations exist (Friston, 2011; Parr et al., 2022).

Postural adjustments initiated by the CNS in response to perturbations can be broadly categorized into anticipatory and compensatory adjustments (Liang et al., 2020). Anticipatory adjustments occur prior to predictable disturbances (Santos et al., 2010), relying on internal models to estimate motion and issue proactive motor commands. Compensatory adjustments are driven by sensory feedback following perturbation onset and include reflexive and voluntary responses to restore balance (Chen et al., 2015; Santos et al., 2010). Although many theories support this internal model-based mechanism (Oman, 1982, 1991), the full process is not yet experimentally confirmed. Validated motion perception models, including the Subjective Vertical Conflict (SVC) (Bos & Bles, 1998) and Multi-Sensory Observer Model (MSOM) (Newman, 2009), are based on the sensory conflict theory, which posits that the CNS continuously updates predicted motion based on feedback to minimize sensory conflict. Despite its relevance, the theory has only recently been incorporated into biomechanical models for head–neck postural stabilization (Happee et al., 2023).

Postural control is critical for maintaining motion comfort, which encompasses both enhancement of ride comfort and mitigation of motion sickness. In AVs, occupants will likely engage in

* Corresponding author.
E-mail address: c.messiou@tudelft.nl (C. Messiou).

https://doi.org/10.1016/j.conengprac.2025.106428
Received 10 January 2025; Received in revised form 26 May 2025; Accepted 26 May 2025
Available online 19 June 2025

non-driving-related tasks such as reading or working (Kyriakidis et al., 2015), reducing their ability to actively stabilize posture. Unpredictable maneuvers may provoke excessive head and body motion (Paddan & Griffin, 1994), leading to increased whole-body vibrations and discomfort (International Organization for Standardization, 1997). Head motion plays a key role in motion perception, particularly through its impact on vestibular and visual systems. Although head motion strongly influences motion sickness (Papaioannou et al., 2023, 2025), most existing models do not predict head or body dynamics. Even when such data is experimentally available, accurate modeling of body-neck-head dynamics is essential to predict responses in new scenarios.

Several head–neck models have been developed, ranging from simple two-pivot systems to complex multi-segment and finite element (FEM) models. Passive models, often used for impact simulations, combine biomechanical detail with simplified representations of active control, and are generally not suitable for simulating postural stabilization (Correia et al., 2020, 2021; Hedenstierna & Halldin, 2008; Meyer et al., 2013). While FEM-based models offer anatomical accuracy, they are computationally intensive, lack integrated postural control algorithms, and are not designed for real-time applications. Other approaches have explored sagittal plane models to study neural mechanisms for head posture stabilization using vestibular and proprioceptive feedback (Fard et al., 2003; Peng et al., 1997, 1999). These models revealed redundancy between feedback sources but were limited in scope, applying only to single-axis or static conditions and using basic control techniques. To date, no existing model integrates advanced postural control algorithms that aim to replicate CNS behavior in minimizing sensory conflict while maintaining head stability in multi-dimensional environments.

The most widely used models in this field are multi-segment models that incorporate detailed anatomical features (Almeida et al., 2009; Brolin et al., 2008; Stemper et al., 2004; Ee et al., 2000). For instance, a recent 3D multi-segment neck model (Happee et al., 2023) combined with MSOM and SVC frameworks estimated head angles and velocities based on sensory feedback and adjusted muscle activity accordingly. Although this approach demonstrated the importance of various feedback pathways, it did not implement a control function explicitly minimizing sensory conflict. Instead, it required tuning of multiple feedback parameters for each condition, limiting its predictive power in new scenarios. Moreover, due to the complexity of the biomechanical structures and feedback loops, such models require high computational effort, making them impractical for applications requiring real-time performance.

To overcome these limitations, this work introduces and employs a Model Predictive Control (MPC) based framework, which offers a principled method for generating control actions by predicting future behavior through an internal model and minimizing a cost function over a finite horizon while satisfying constraints. In this framework, the cost function represents a plausible CNS objective: minimizing both sensory conflict and muscle effort under biomechanical constraints. The internal prediction model is continuously updated using real-time sensory feedback, aligning the approach with current theories of CNS behavior. This MPC-based control is implemented in a simplified biomechanical model – a double inverted pendulum – representing the head and neck system. The model includes multiple sensory pathways (muscle effort, somatosensory input, semicircular canal, and otolith feedback) and simulates compensatory postural responses during anterior–posterior and pitch perturbations under eyes-closed conditions. Validation is performed against experimental human data from scenarios specifically designed to excite the head–neck system in the sagittal plane. A schematic of this concept is shown in Fig. 1. By focusing on postural control, this work extends previous applications of MPC (Cole, 2018; Fieldhouse & Cole, 2024), which used sensory predictions (Gaussian process model) combined with sensory feedback through a Kalman filter to model the drivers' perception and update vehicle state estimates in a path-following context. To the authors' knowledge, there is no work in the literature adopting MPC in head–neck modeling, except for an earlier exploration presented by the authors in a conference paper (Messiou et al., 2023).

Table 1
Neck and head dimensions, mass, moments of inertia and centers of mass.

	Neck	Head
Depth (m)	0.0589	0.0995
Width (m)	0.0589	0.0700
Height (m)	0.0994	0.1344
Mass (kg)	1.6000	6.2300
MoI_x (kg m^2)	0.0069	0.0180
MoI_y (kg m^2)	0.0069	0.0230
MoI_z (kg m^2)	0.0022	0.0170
CoM_x (m)	0.0000	0.0000
CoM_y (m)	0.0000	0.0000
CoM_z (m)	0.0000	0.0000

The key contributions of this study are as follows:

- This study introduces the first MPC-based postural control framework that integrates plausible CNS behavior, including modeling of neural store and real-time sensory feedback, to minimize sensory conflict during stabilization.
- The influence of different sensory pathways (muscle effort, somatosensory input, semicircular canals, and otoliths) on the model's predictive accuracy and computational efficiency is evaluated.
- It is demonstrated that a single optimized MPC configuration can generalize across different perturbation types, offering a computationally efficient alternative to complex multi-segment models.

2. System dynamics: Plant and prediction model

This section outlines (a) the plant: a simplified head–neck model in Simscape, and (b) the prediction model: Ordinary Differential Equations (ODEs) describing the system dynamics.

2.1. Plant: Simscape model

The head–neck model (Fig. 2) was developed using MATLAB's Simscape Multibody, which uses blocks to represent bodies, joints, forces, and sensors. For each body, mass, inertia, and geometry are defined, while joints specify DoFs, actuation, and internal mechanics (e.g., stiffness, damping). Simscape formulates and solves the system's equations of motion. The model includes three main body segments: (1) two ellipsoidal bodies representing the head and the neck, and (2) a rectangular block representing the lumped torso and the car. Perturbations are applied to the rectangular block body, approximated as the T1 vertebra location, i.e. the first of twelve vertebrae of the thoracic spinal column. Each segment includes dimensions, moments of inertia (MoI), and centers of mass (CoM) The MoI are calculated based on segment geometry and the rotational radius between the CoM and joints. The CoM is positioned at the center of each segment, with dimensions specified according to the GEBOD regression equations (Cheng et al., 1994). Tables 1 and 2 show the model anthropometric parameters, assuming a male with 83 kg weight and 1.80 m standing height.

Joint locations are also determined based on the GEBOD regression equations, with J1 and J2 (neck joints) being implemented as 3DoF gimbal joints with translation blocked. The T1-world joint retains 6DoF to allow general input motion. This study focuses on sagittal plane perturbations. Furthermore, built-in Simscape sensors (e.g., rigid transformations between body and world frames, as well as joint sensors) are used to update the plant's states at every simulation timestep (T_{sim}). T_{sim} is defined as the time step between each simulation step when running the proposed framework (Fig. 1) online in Simulink. The plant's states are equivalent to those used by the prediction model.

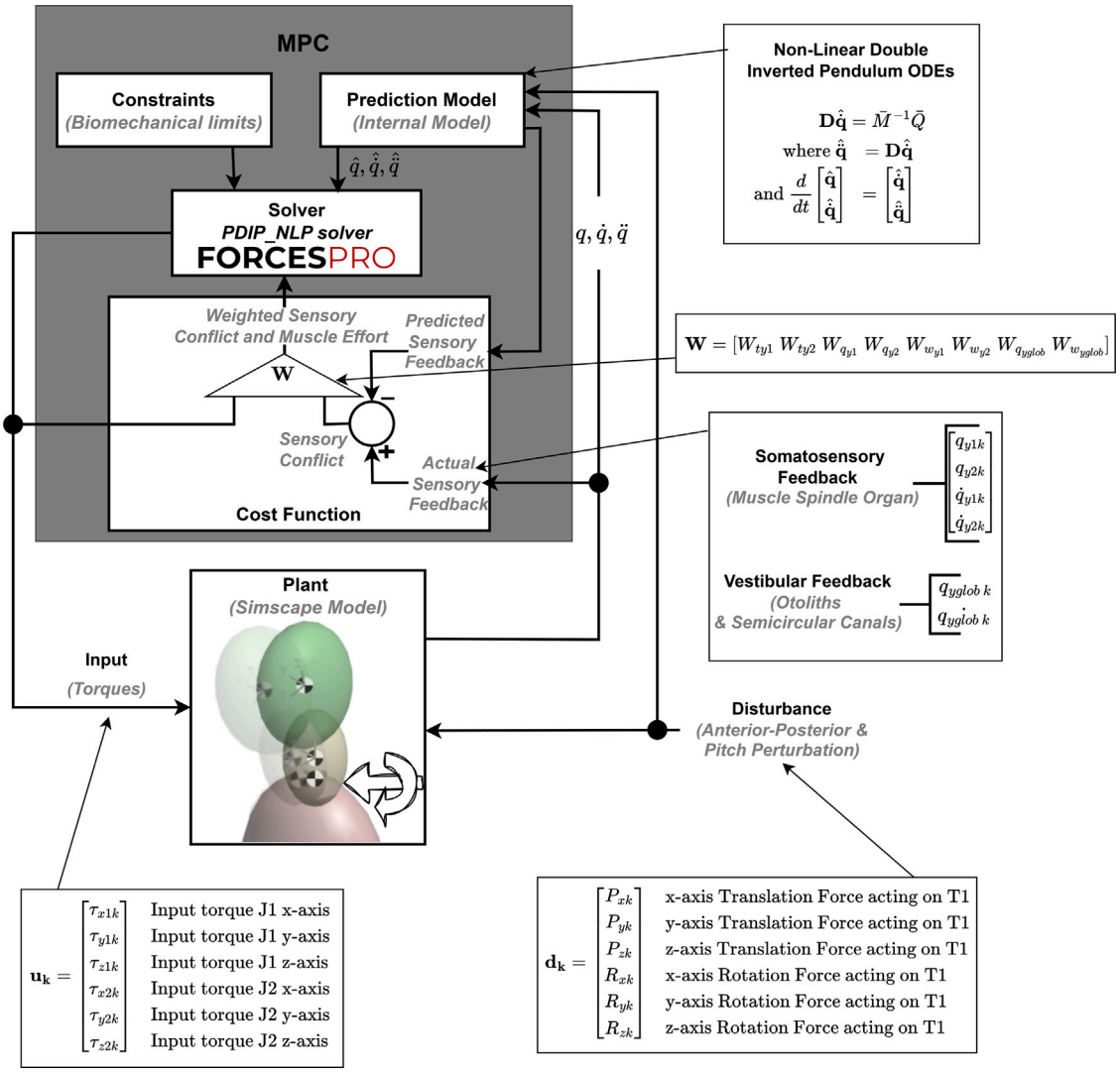

Fig. 1. Block diagram of the postural stabilization system illustrating the CNS's function using MPC. When the Simscape model experiences a disturbance ($d_k(T_{sim})$) at time step $k = 1$ and simulation timestep $T_{sim} = 8$ ms, the CNS receives sensory feedback through afferent pathways: proprioceptive (muscle spindles and Golgi tendons), vestibular (semicircular canals and otolith organs), and visual inputs. In this study, this sensory feedback is derived from the Simscape model's states ($q(T_{sim}), \dot{q}(T_{sim}), \ddot{q}(T_{sim})$). The MPC internal model predicts sensory outcomes ($\hat{q}_k(T_{sim}), \hat{\dot{q}}_k(T_{sim}), \hat{\ddot{q}}_k(T_{sim})$) over a prediction horizon ($k = 1, 2, \ldots, 20$) using the Prediction Model's ODEs (Section 2.2). The MPC solver adjusts motor commands by minimizing sensory conflict (difference between predicted and actual feedback) and muscle effort, while adhering to biomechanical constraints. These control actions are applied to the plant ($u_k(T_{sim})$) at time step $k = 1$ to mimic CNS-inspired postural stabilization.

Table 2
Neck and head joint locations.

	Joint Locations
Upper neck joint (J2)	Relative to CoM of head:
$J2_x$ (m)	0.0270
$J2_y$ (m)	0.0000
$J2_z$ (m)	0.1344
Lower neck joint (J1)	Relative to CoM of neck:
$J1_x$ (m)	0.0000
$J1_y$ (m)	0.0000
$J1_z$ (m)	0.0406

2.2. Prediction model

The MPC prediction model (Fig. 1) uses ODEs to represent the plant's nonlinear dynamics, solved over a prediction horizon (N)with discretization interval (T_{sp}). The model is a double inverted pendulum, derived using GEBOD anthropometric parameters for a 50th percentile male, and includes masses (m_i), lengths (l_i), joint-CoM distances (r_i), and MoIs ($I_{xx\,i}$, $I_{yy\,i}$, $I_{zz\,i}$) for torso ($i = 0$), neck ($i = 1$), and head ($i = 2$).

The system has 12 DoFs, accounting for both rotation and translation. To reduce computation time (RTF), the TMT multibody method in 3D (Schwab & L., 2020) is used, which provides a compact formulation.

External forces and control inputs

The total external force vector $\mathbf{F}(t)$, consisting of applied perturbations at T1 and MPC control inputs, is given by:

$$\mathbf{d}(t) = \begin{bmatrix} P_x(t) \\ P_y(t) \\ P_z(t) \\ R_x(t) \\ R_y(t) \\ R_z(t) \end{bmatrix} \mathbf{u}(t) = \begin{bmatrix} \tau_{x1}(t) \\ \tau_{y1}(t) \\ \tau_{z1}(t) \\ \tau_{x2}(t) \\ \tau_{y2}(t) \\ \tau_{z2}(t) \end{bmatrix} \tag{1}$$

$$\mathbf{F}(t) = [\mathbf{d}(t); \mathbf{u}(t)] \tag{2}$$

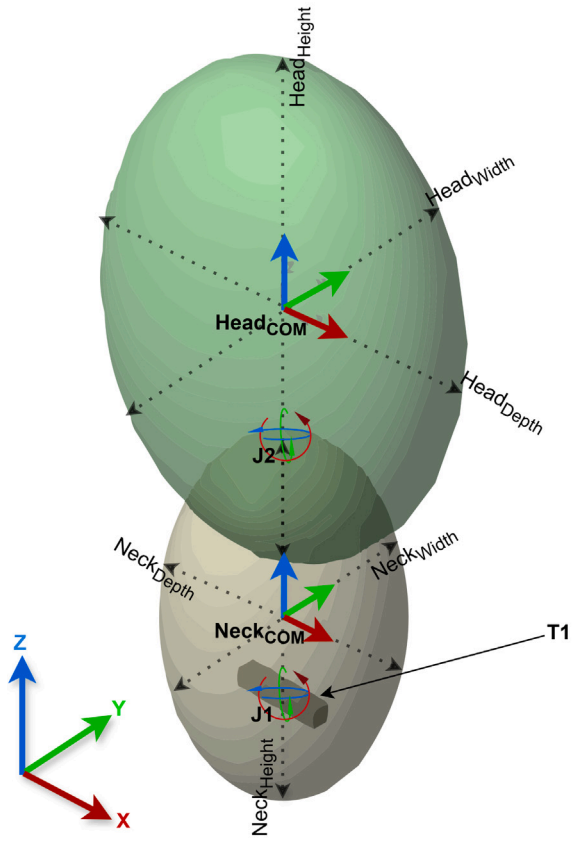

Fig. 2. Head–neck model with global and local coordinate frames at the initial frame (upright).

where:

- P_x, P_y, P_z are translational perturbations applied at T1.
- R_x, R_y, R_z are rotational perturbations.
- $\tau_{xi}, \tau_{yi}, \tau_{zi}$ are control torques applied at joints $i = 1, 2$.

State-space representation

The generalized coordinates ($\hat{q}$) and their derivatives ($\dot{\hat{\mathbf{q}}}$), are given as:

$$\hat{\mathbf{q}}(t) = \begin{bmatrix} \hat{x_0}(t) \\ \hat{y_0}(t) \\ \hat{z_0}(t) \\ \hat{q_{x0}}(t) \\ \hat{q_{y0}}(t) \\ \hat{q_{z0}}(t) \\ \hat{q_{x1}}(t) \\ \hat{q_{y1}}(t) \\ \hat{q_{z1}}(t) \\ \hat{q_{x2}}(t) \\ \hat{q_{y2}}(t) \\ \hat{q_{z2}}(t) \end{bmatrix}, \quad \dot{\hat{\mathbf{q}}}(t) = \begin{bmatrix} \dot{\hat{x_0}}(t) \\ \dot{\hat{y_0}}(t) \\ \dot{\hat{z_0}}(t) \\ \dot{\hat{q_{x0}}}(t) \\ \dot{\hat{q_{y0}}}(t) \\ \dot{\hat{q_{z0}}}(t) \\ \dot{\hat{q_{x1}}}(t) \\ \dot{\hat{q_{y1}}}(t) \\ \dot{\hat{q_{z1}}}(t) \\ \dot{\hat{q_{x2}}}(t) \\ \dot{\hat{q_{y2}}}(t) \\ \dot{\hat{q_{z2}}}(t) \end{bmatrix} \tag{3}$$

where:

- $\hat{q}_{xi}, \hat{q}_{yi}, \hat{q}_{zi}$ represent joint angles for the torso ($i = 0$), neck ($i = 1$), and head ($i = 2$).
- $\hat{x_0}, \hat{y_0}, \hat{z_0}$ define global translational positions of the base (T1).

Rotation matrices (R) are then constructed as the product of axis-specific rotations (R_{xi}, R_{yi}, R_{zi}) and depend on the angular displacements $\hat{q}_{xi}, \hat{q}_{yi}, \hat{q}_{zi}$. The mass ($M_i$) and inertia ($I_i$) matrices for each body are represented as diagonal matrices:

$$M_i = \text{diag}(m_i, m_i, m_i), \tag{4}$$

$$I_i = \text{diag}(I_{xxi}, I_{yyi}, I_{zzi}) \tag{5}$$

Transformation matrices (T_i) are derived as Jacobians of the position vectors with respect to the generalized coordinates:

$$T_i = \frac{\partial u_i}{\partial \hat{q}}, \tag{6}$$

where u_i represents the displacement fields of the system components. The generalized mass matrix is formulated as:

$$\bar{M} = \sum_{i=0}^{2} (T_i^\top M_i T_i + \mathbf{B}_1^\top I_i \mathbf{B}_i) \tag{7}$$

where B_i represent the rate of orientation transformation matrices in body frames. The generalized force vector combines external forces acting on the CoM for each body ($F_{\text{ext}i}$), convective terms (h_i, g_i), and external moments ($M_{\text{ext}i}$):

$$\bar{Q} = F + \sum_{i=0}^{2} (T_i^\top (F_{\text{ext},i} - M_i h_i) + B_i^\top (M_{\text{ext},i} - I_i g_i - w_i \times (I_i w_i))) \tag{8}$$

The equations of motion for the double derivatives of the generalized coordinates ($\ddot{\hat{\mathbf{q}}}$) are then expressed as:

$$\mathbf{D}\ddot{\hat{\mathbf{q}}} = \bar{M}^{-1} \bar{Q} \tag{9}$$

$$\text{where } \dot{\hat{\mathbf{q}}} = \mathbf{D}\hat{\mathbf{q}} \tag{10}$$

The generalized state vector is finally expressed as:

$$f(\hat{\mathbf{x}}, \mathbf{u}, \mathbf{d}) = \frac{d}{dt} \begin{bmatrix} \hat{q} \\ \dot{\hat{q}} \end{bmatrix} = \begin{bmatrix} \dot{\hat{q}} \\ \ddot{\hat{q}} \end{bmatrix}. \tag{11}$$

where $\hat{\mathbf{x}}$ are the plant's states. The full ODE derivations are provided in the online supplementary material.

3. MPC-based postural control

In this work, MPC is employed to represent the behavior of the CNS. The control framework (Fig. 1) consists of the FORCESPRO MPC Block (controller) and the Simscape model (Plant, Section 2.1), with input perturbations acting as external forces (Eq. (1)). At each T_{sim}, the MPC block receives the actual plant states and state derivatives ($q, \dot{q}, \ddot{q}$ - Fig. 1), current 6DoF perturbations (translational and rotational, Eq. (1)), and the weight vector for the cost functions (Section 3.3). The Simscape model continuously updates the actual states, which are used to initialize the first step of the MPC's prediction model (Section 2.2). This prediction model forecasts the motion over the selected prediction horizon (Section 3.4). The solver (Section 3.5) computes the optimal control torques at each T_{sim}, considering the internal prediction model, constraints (Section 3.2), and cost function (Section 3.3). Both the Simscape and prediction model start from zero initial states, corresponding to an upright posture at the beginning of the simulation.

3.1. Problem formulation

The MPC problem for head–neck postural stabilization is formulated as a constrained nonlinear optimization problem. The objective function minimizes sensory conflict and muscle effort while ensuring biomechanical constraints are satisfied. The general form of the MPC problem is:

$$\min_{\mathbf{u}} J = \sum_{k=0}^{N} \ell(\hat{\mathbf{x}}_k, \mathbf{x}, \mathbf{u}_k) \tag{12}$$

where J is the total cost over the prediction horizon N, $\hat{\mathbf{x}}_k$ is the prediction model states at time step k, $\mathbf{x}$ is the plant states at $k = 1$, $\mathbf{u}_k$ is the control input and the stage cost $\ell(\hat{\mathbf{x}}_k, \mathbf{x}, \mathbf{u}_k)$ is defined in Eq. (22).

Subject to:

State dynamics (Section 2.2) discretized for compatibility with the MPC solver:

$$\hat{\mathbf{x}}_{k+1} = f(\hat{\mathbf{x}}_k, \mathbf{u}_k, \mathbf{d}_k) \tag{13}$$

State and Control equality constraints (Section 3.2):

$$\hat{\mathbf{x}}_{\min} \leq \hat{\mathbf{x}}_k \leq \hat{\mathbf{x}}_{\max} \tag{14}$$

$$\mathbf{u}_{\min} \leq \mathbf{u}_k \leq \mathbf{u}_{\max} \tag{15}$$

Global head–neck system inequality constraints (biomechanical limits):

$$\mathbf{h}_{\hat{x}}(\hat{\mathbf{x}}_k) \leq \mathbf{0} \tag{16}$$

$$\mathbf{h}_{u}(\mathbf{u}_k) \leq \mathbf{0} \tag{17}$$

where the state-dependent constraint vector $\mathbf{h}_{\hat{x}}(\hat{\mathbf{x}}_k)$ encodes limits on global head angle and global head angular velocity:

$$\mathbf{h}_{\hat{x}}(\hat{\mathbf{x}}_k) = \begin{bmatrix} q_{yg\hat{lob}\,k} - q_{yg\hat{lob},\max} \\ q_{yg\hat{lob},\min} - q_{yg\hat{lob}\,k} \\ q_{yg\hat{\dot{lob}}\,k} - q_{yg\hat{\dot{lob}},\max} \\ q_{yg\hat{\dot{lob}},\min} - q_{yg\hat{\dot{lob}}\,k} \end{bmatrix} \leq \mathbf{0} \tag{18}$$

where:

$$q_{yg\hat{lob}\,k} = q_{y\hat{0}\,k} + q_{y\hat{1}\,k} + q_{y\hat{2}\,k}$$

$$q_{yg\hat{\dot{lob}}\,k} = q_{y\hat{\dot{0}}\,k} + q_{y\hat{\dot{1}}\,k} + q_{y\hat{\dot{2}}\,k}$$

Similarly, the control-dependent constraint vector $\mathbf{h}_u(\mathbf{u}_k)$ captures the limit on the total muscle torque acting in flexion/extension:

$$\mathbf{h}_{u}(\mathbf{u}_k) = \begin{bmatrix} \tau_{yglob\,k} - \tau_{yglob,\max} \\ \tau_{yglob,\min} - \tau_{yglobyglob,\,k} \end{bmatrix} \leq \mathbf{0} \tag{19}$$

where:

$$\tau_{yglob\,k} = \tau_{y1\,k} + \tau_{y2\,k}$$

Prediction horizon:

The MPC operates over a finite forecast horizon, defined as:

$$T_H = N \times T_{sp} \tag{20}$$

where N is the prediction horizon and T_{sp} is the discretization timestep.

This general formulation captures the CNS-inspired postural control strategy. The specific components of the MPC – constraints, cost function, prediction horizon, and solver – are detailed in the following sections. As this paper focuses on the sagittal plane, the formulation is limited to the costs and constraints on the states, control inputs, and model responses relevant to sagittal head–neck motion.

3.2. Constraints

The constraints on states and control inputs are established based on biomechanical limits to ensure realistic simulation of the head–neck dynamics. More specifically, they reflect the physiological limits of cervical spine motion and muscle forces.

Cervical Spine Flexion/Extension: Typical values range from 45–50° for flexion and 60–70° for extension (Moriguchi et al., 2011). These limits accommodate normal perturbation scenarios in dynamic driving, excluding extreme impact conditions.

Angular Velocity: The peak angular velocity for cervical flexion and extension can reach approximately 20 rad/s, varying based on individual and task-specific conditions (Tierney et al., 2019).

Neck Flexion/Extension Forces: The maximum forces for neck flexion are about 16 N m for females and 34 N m for males. For neck extension, the values are higher, averaging 34 N m for females and 60 N m for males (Lo Martire et al., 2017).

These constraints are used to satisfy the average data from the studies (Section 4) and were adjusted for a 50th percentile male, reflecting the demographics of the experimental datasets used to validate the model's responses to rotational and translational trunk perturbations in the sagittal plane. Accordingly, the above values were used to define inequality constraints for global angles, angular velocities, and torques, and equality constraints to define the upper ($\mathbf{u}_{max}, \hat{\mathbf{x}}_{max}$) and lower bounds ($\mathbf{u}_{min}, \hat{\mathbf{x}}_{min}$) for each state ($\hat{\mathbf{x}}_k = [\hat{q}_{y1}, \hat{q}_{y2}, \hat{\dot{q}}_{y1}, \hat{\dot{q}}_{y2}]$) and control input ($\mathbf{u}_k = [\tau_{y1}, \tau_{y2}]$). For the sagittal plane perturbations in this study, the relevant equality constraints (as denoted in Eqs. (14) & (15)) are:

$$\begin{bmatrix} -30 \\ -30 \\ -\frac{\pi}{5} \\ -\frac{\pi}{5} \\ -\frac{\pi}{20} \\ -\frac{\pi}{20} \end{bmatrix} \leq \begin{bmatrix} \tau_{y1} \\ \tau_{y2} \\ \hat{q}_{y1} \\ \hat{q_{y2}} \\ \hat{\dot{q}}_{y1} \\ \hat{\dot{q}}_{y2} \end{bmatrix} \leq \begin{bmatrix} 15 \\ 15 \\ \frac{\pi}{5} \\ \frac{\pi}{5} \\ \frac{\pi}{15} \\ \frac{\pi}{15} \end{bmatrix} \tag{21}$$

where τ_{y1} is input torque J1 about y-axis (N m); τ_{y2} is input torque J2 about y-axis (N m); $\hat{q_{y1}}$ is y-angle of J1 (rad); $\hat{q_{y2}}$ is y-angle of J2 (rad); $\hat{\dot{q}}_{y1}$ is y-angular velocity of J1 (rad/s) and $\hat{\dot{q}}_{y2}$ is y-angular velocity of J2 (rad/s).

3.3. Cost functions

The cost function in the MPC-based postural control algorithm addresses the mismatch between predicted and actual sensory inputs representing a plausible CNS objective i.e., to minimize sensory conflict and muscle effort. The predicted sensory feedback ($\hat{q}, \hat{\dot{q}}, \hat{\ddot{q}}$) is generated by the internal prediction model, while the actual feedback is extracted from the Simscape model ($q, \dot{q}, \ddot{q}$). The mismatch is penalized over the prediction horizon, with each component weighted accordingly.

This approach mimics the CNS's hypothesized internal model mechanism, in which motor output is continuously refined by comparing predicted and actual sensory states. The model includes feedback pathways that replicate somatosensory and vestibular inputs—specifically, Golgi tendon organ (muscle effort/toque), muscle spindles (joint angles and velocities), semicircular canal signals (angular velocity), and otolith signals (tilt/verticality). These components have been shown to be essential in stabilizing posture under dynamic, eyes-closed conditions (Happee et al., 2023).

The cost function includes eight weighted terms:

1. Muscle torque effort at the lower and upper neck joints ($\tau_{y1\,k}$-F1, $\tau_{y2\,k}$-F2), representing Golgi tendon organ feedback.
2. Relative angular positions (q_{y1}-F3 q_{y2}-F4) and velocities ($\dot{q_{y1}}$-F5 $\dot{q_{y2}}$-F6), simulating muscle spindle input.
3. Global head angular velocity and tilt ($q_{yg\hat{\dot{lob}}\,k}$-F9, $q_{yg\hat{lob}\,k}$-F7), corresponding to semicircular canal and otolith organ feedback.

Eq. (22) presents the complete cost function for which the cost is minimized over N. Each component is squared and multiplied by a respective weight (W), which reflects the possible prioritization of sensory channels during postural stabilization. These weights were tuned using a high-level optimization process to match experimental data across multiple perturbation conditions.

In this implementation, visual feedback is excluded to isolate and evaluate the impact of non-visual sensory pathways. The simplified head–neck model has two sagittal-plane rotational DoFs, corresponding to joints J1 and J2. By minimizing this cost function under biomechanical constraints, the MPC replicates CNS-like stabilization without requiring the complex tuning of feedback gains seen in other models.

3.4. Prediction horizon

In optimizing the horizon N, a critical balance had to be struck between computational efficiency and head–neck model accuracy. Due

$$J = \sum_{k=0}^{N} \ell(\hat{\mathbf{x}}_k, \mathbf{x}, \mathbf{u}_k)$$

$$= \begin{bmatrix} W_{ty1} \cdot \|\tau_{y1\,k}\|^2 + & \text{Torque for J1 (F1)} \\ W_{ty2} \cdot \|\tau_{y2\,k}\|^2 + & \text{Torque for J2 (F2)} \\ W_{q_{y1}} \cdot \|\hat{q_{y1}}_k - q_{y1}\|^2 + & \text{Angle about J1 (F3)} \\ W_{q_{y2}} \cdot \|\hat{q_{y2}}_k - q_{y2}\|^2 + & \text{Angle about J2 (F4)} \\ W_{w_{y1}} \cdot \|\hat{\dot{q}_{y1}}_k - \dot{q_{y1}}\|^2 + & \text{Angular velocity about J1 (F5)} \\ W_{w_{y2}} \cdot \|\hat{\dot{q}_{y2}}_k - \dot{q_{y2}}\|^2 + & \text{Angular velocity about J2 (F6)} \\ W_{q_{yglob}} \cdot \|\hat{q_{yglob}}_k - q_{yglob}\|^2 + & \text{Head global angle (F7)} \\ W_{w_{yglob}} \cdot \|\hat{\dot{q}_{yglob}}_k - \dot{q_{yglob}}\|^2 & \text{Head global angular velocity (F8)} \end{bmatrix} \tag{22}$$

to the complexity and nonlinearity of the ODEs, an increased N could increase the computational load, thus increasing the RTF. However, a too small N could compromise the accuracy and robustness of the system's response. Through testing (Appendix B) an optimal setup was identified: a T_{sp} of 10 ms with one intermediate shooting node per interval, and a T_H configured to 200 ms by setting N to 20.

3.5. MPC solver

For the MPC solver, FORCESPRO was used, an off-the-shelf optimization tool suited for the development of highly customized solvers (Zanelli et al., 2017). It was selected for its ability to handle large ODE systems and its efficient matrix handling via the *MX* class, essential for the prediction model. FORCESPRO employs CASADI's Automatic Differentiation (versions 3.5.1–3.5.5) and supports multicore computation via OpenMP, enabling efficient distribution of computational load across cores. The Nonlinear Primal–Dual Interior-Point method ('PDIP_NLP') was chosen for its robustness to solve the problem defined in Section 3.1, with the internal continuous-time system dynamics integrated using a 4th-order explicit Runge–Kutta method. Details of the complete FORCESPRO configuration are provided in Appendix A.

4. Scenarios: Experimental datasets from human subjects

The validation of the head–neck model against experimental data involves two distinct scenarios with applied body motion in seated human subjects: anterior–posterior perturbation (Scenario A) (Forbes et al., 2013) and pitch perturbation (Scenario B) (Keshner et al., 1995). These experimental datasets from the literature were specifically selected, because they were uniquely designed to excite the human head–neck system within the bandwidth relevant to ride comfort and to extract frequency response functions between the trunk (the point of perturbation application) and the head/neck. Consequently, these experimental datasets are ideally suited for head–neck model fitting and validation (Happee et al., 2019).

Scenario A involves fore-aft translational pseudorandom multisine perturbations applied to a seat using a motion platform. The bandwidth for these perturbations was 0.3–8.0 Hz. Participants were restrained by a five-point harness on a rigid seat with a 10° inclined backrest and listened to a science radio program to minimize voluntary responses.

Scenario B applied pseudorandom multisine seat pitch rotations around the interaural axis, and included three conditions: Voluntary Stabilization (VS), No Vision (NV), and Mental Arithmetic (MA). For the purposes of this study, the MA condition was employed, where participants performed mental arithmetic tasks to divert focus from head stabilization. This condition was chosen to simulate natural responses in situations where occupants of automated vehicles would not actively attempt to stabilize their heads, while engaged in NDRTs. The bandwidth for these perturbations was 0.35–3.05 Hz.

The averaged responses of the participants were used to tune and validate the model. Averaging responses mitigates the influence of individual variability and outliers, resulting in a more robust and generalizable model that better represents the collective biomechanical response to these perturbations. The eyes-closed condition from both scenarios was used for validation, as it simplifies the interpretation of results by isolating vestibular and somatosensory influences while excluding visual feedback. The validation step assesses the predictive capabilities of the model by comparing its head responses under sagittal plane excitation at T1 (trunk), both in translation (scenario A) and rotation (scenario B) with human experimental data.

5. High-level optimization: Parameter tuning

In addition to the low-level optimization of the MPC for control input computation, a high-level optimization was implemented to tune the MPC cost function weights. This section outlines the high-level optimization process, the configuration used for each scenario, and the fine-tuning of evaluation functions in Scenario A. The objective was to optimize the MPC weights in the cost function to fit the simulated head–neck model responses with the averaged human responses from two experimental studies (Section 4). Each cost function component (Eq. (22)) is scaled by a weight, influencing the MPC solver's prioritization during low-level optimization. The high-level optimization is formulated as follows:

$$\min_{\mathbf{W}} f(Feval1(\mathbf{W}), \ldots, Fevali(\mathbf{W})) = \sqrt{\mathbb{E}\left[(X^S_{i,\text{sim}} - X^S_{i,\text{exp}})^2\right]} \tag{23}$$

where $X_{i,\text{sim}}$ is the simulated model head response and $X_{i,\text{exp}}$ is the human head response; S is the perturbation scenario; $\mathbf{W}$ is the weight vector shown in Fig. 1. The index i corresponds to the evaluation metrics (Feval) that compute the root mean squared error (RMSE) between the simulated and experimental head responses in both the time and frequency domains (Eqs. (24), (25)). For the high level optimization, multi-objective genetic algorithms were employed using MATLAB's *multiga()* function. The initial population matrix (*'x1'*) of size $[n \times 20]$, where n is the number of optimization variables, was generated by randomizing best-case values from preliminary analyses. The population size was set to 200. Additionally, the impact of different components in the MPC cost function was examined as part of the low-level optimization. The influence of different cost function components on low-level optimization was further analyzed using random forests. Cost function components were grouped into distinct "cases" to analyze their influence on head–neck responses. This approach provides insights into how each feedback pathway influences the head–neck model's response and validates the relevance of incorporating these pathways in replicating CNS-driven postural control.

5.1. Configuring the high-level optimization

The human experimental datasets from Section 4 are used in the high-level optimization to fit the model responses with real human responses. This section details the optimization configuration for Scenarios A, B, and C.

Table 3
Correlation coefficient ($\rho_{\text{Feval}_i,\text{Feval}_j}$) between Fevals. The colors depict the following levels of ρ: (a) red: $\rho = 1$, (b) orange: $0.9 < \rho < 1$, (c) yellow: $0.7 < \rho \leq 0.9$, (d) blue: $\rho \leq 0.7$, (e) gray: values below the diagonal.

	Feval1	Feval2	Feval3	Feval4	Feval5	Feval6	Feval7	Feval8
Feval1:qy (rad)	1.00	0.714	0.762	0.670	0.633	0.733	−0.084	−0.049
Feval2:x (m)	0.00	1.00	0.201	0.996	−0.054	0.997	−0.073	0.003
Feval3:wy (rad/s)	0.00	0.00	1.00	0.151	0.942	0.213	−0.060	−0.059
Feval4:vx (m/s)	0.00	0.00	0.00	1.00	−0.110	0.992	−0.071	0.004
Feval5:$\|f_{qy}\|$ (deg/m)	0.00	0.00	0.00	0.00	1.00	−0.034	−0.034	−0.063
Feval6:$\|f_x\|$ (m/m)	0.00	0.00	0.00	0.00	0.00	1.00	−0.071	−0.003
Feval7:$\angle f_{qy}$ (deg)	0.00	0.00	0.00	0.00	0.00	0.00	1.00	−0.064
Feval8:$\angle f_x$ (deg)	0.00	0.00	0.00	0.00	0.00	0.00	0.00	1.00

5.1.1. Scenario A: Anterior-posterior perturbation

Scenario A optimization utilized eight evaluation functions based on RMSE between simulated and experimental data in both time and frequency domains. The experimental dataset included head rotation and translation, allowing comprehensive evaluation. The responses considered for anterior–posterior (AP) perturbation are:

$$Feval1-8 = \left[\sqrt{\mathbb{E}[(\Delta X_1^{AP})^2]}, \ldots, \sqrt{\mathbb{E}[(\Delta X_8^{AP})^2]}\right] \tag{24}$$

where: $X_1^{AP} = q_y$ (head global pitch in time domain), $X_2^{AP} = x$ (head global linear position in time domain), $X_3^{AP} = w_y$ (head global angular velocity in time domain), $X_4^{AP} = v_x$ (head global linear velocity in time domain), $X_5^{AP} = \|f_{qy}\|$ and $X_6^{AP} = \|f_x\|$ (gains of head global pitch and linear position in frequency domain), $X_7^{AP} = \angle f_{qy}$ and $X_8^{AP} = \angle f_x$ (phases of head global pitch and linear position in frequency domain).

To calculate Feval5-Feval8, the T1-to-head transmission of the perturbation stimulus were estimated. More specifically, two transfer functions were estimated: (1) between the observed signal at T1 (input) and the head's global pitch (output), and (2) between the observed signal at T1 (input) and the head's global position (output). The gain and phase of the system were computed using a custom method specifically designed to analyze the multisine input signals in Scenario A. This method utilizes a predefined frequency vector to focus on the frequencies of interest, which in this case correspond to the harmonics of the multisine signal used in Forbes et al. (2013) to excite seated human subjects (Section 4): $f = [0.25, 0.65, 1.05, 1.45, 1.85, 2.25, 2.7, 3.2, 3.85, ..4.65, 5.55, 6.65, 8]$ Hz, adjusted with additional offsets and scaled by the experiment's fundamental time period (20 s). Through this approach, the method computes spectral densities and the transfer functions only at these specific frequencies, ensuring no interference from irrelevant spectral components. Furthermore, frequency averaging is applied to improve signal-to-noise ratio while preserving the distinct characteristics of the multisine excitation.

All eight evaluation functions were included in the optimization process to ensure an effective tuning of the MPC weights. After an initial optimization, correlation coefficients (Lindroth et al., 2010) were calculated to efficiently configure the evaluation functions and avoid inconsiderable selection of them (Papaioannou & Koulocheris, 2018). Based on the correlation coefficients (Table 3), it became evident that some of these functions were highly correlated, with correlation coefficients ≥ 0.9. Such high correlations suggest that these functions provide redundant information, and could make the optimization process ineffective while delaying the convergence. Hence, Feval4, Feval5 and Feval6 were excluded from Scenario C optimization. This will improve the ratio between Fevals for Scenario A (5 Fevals after exclusion) and Scenario B (2 Fevals), decreasing the bias of the high-level optimization due to unbalanced evaluation functions.

5.1.2. Scenario B: Pitch perturbation

Scenario B optimization focused solely on frequency-domain evaluation due to the lack of time-domain experimental data. The evaluation functions considered for pitch (P) perturbation are:

$$Feval9-10 = \left[\sqrt{\mathbb{E}[(\Delta X_1^{P})^2]}, \sqrt{\mathbb{E}[(\Delta X_2^{P})^2]}\right] \tag{25}$$

where $X_1^P = \|f_{qy}\|$ (gain of head global pitch in frequency domain), $X_2^P = \angle f_{qy}$ (phase of head global pitch in frequency domain).

The gain and phase of the system were computed in the frequency domain using a custom implementation of the transfer function estimation tailored to Scenario B's multisine input perturbation applied to seated participants (Keshner et al., 1995), as described in Section 4. The method extracts system characteristics at the predefined frequencies of interest ($f2 = [0.3, 0.7, 1.5, 2.1, 3.1]$ Hz) from the broader frequency spectrum. After performing a Fast Fourier Transform (FFT) on both the input signal (T1 global pitch) and the output signal (head global pitch), the spectral densities were computed. The transfer function gain and phase were then derived using these spectral densities. Only the spectral components corresponding to the target frequencies ($f2$) were extracted.

5.1.3. Scenario C: Multi-scenario optimization

In the multi-scenario (Scenario C) optimization, both anterior–posterior and pitch perturbations were optimized simultaneously to derive a single set of weights applicable to both conditions. A total of seven evaluation functions were used: five from Scenario A (Feval1–Feval3 and Feval7–Feval8) and two from Scenario B (Feval9 and Feval10)".

5.2. Configuring MPC-tuning process

One of the main objectives of this study was to evaluate the impact of the different feedback pathways (muscle effort, somatosensory, semicircular and otolith) on the head–neck model's performance, including both accuracy and computational efficiency. Additionally, the analysis aimed to determine whether the importance of each component of the cost function varied between scenarios A and B.

This was accomplished by initially optimizing the MPC-based postural control using the full set of pathways (Section 3.3) – muscle effort, somatosensory, semicircular, and otolith – for both scenarios. Optimization was carried out following the same procedure outlined above for both scenarios. To assess the influence of each component of the cost function on the head–neck model's response, Random Forests were employed to calculate the importance of each cost function component with respect to the evaluation functions and the RTF. Feature importance was calculated using Mean Decrease in Accuracy (Permutation Importance), which evaluates the impact on head–neck model accuracy when the values of a feature are randomly shuffled. A larger decrease in accuracy signifies greater importance.

Table 4 displays the feature importance of the evaluation functions (Fevals) of the genetic algorithm optimization for Scenario A (Feval1 - Feval8) and Scenario B (Feval9 - Feval10) (Section 5). The table also shows the RTF for each scenario relative to the cost function weights. The results indicate that relative angles and otolith feedback have

Table 4
Feature importance for cost function weights vs. Feval1 - Feval8 and RTF for Scenario A and Feval9-Feval10 and RTF for Scenario B.

Feature importance	W_{ty1}	W_{ty2}	$W_{q_{y1}}$	$W_{q_{y2}}$	$W_{w_{y1}}$	$W_{w_{y2}}$	W_{qglob}	W_{wglob}
Feval1:qy (rad)	1.65	0.56	−0.02	0.11	3.49	2.16	0.13	0.53
Feval2:x (m)	2.33	0.35	0.20	−0.01	0.97	2.91	0.18	0.73
Feval3:wy (rad/s)	0.30	2.24	−0.14	0.27	3.84	0.97	0.05	0.26
Feval4:vx (m/s)	2.31	0.50	0.22	0.04	0.72	2.76	0.26	0.63
Feval5:$\|f_{qy}\|$ (deg/m)	0.09	0.76	0.05	−0.04	2.43	2.73	0.13	0.16
Feval6:$\|f_{qy}\|$ (m/m)	0.77	1.08	0.15	−0.08	0.48	1.34	0.28	0.62
Feval7:$\angle f_{qy}$ (deg)	0.01	0.32	−0.01	0.01	−0.03	0.77	0.01	0.11
Feval8: $\angle f_x$ (deg)	−0.03	0.05	−0.01	0.18	0.16	0.25	−0.06	0.03
RTF	2.71	1.07	0.26	−0.12	0.96	0.91	0.01	0.16
Feval9:$\|f_{qy}\|$ (deg/deg)	2.78	0.77	0.47	0.55	1.82	2.48	0.56	0.91
Feval10:$\angle f_{qy}$ (deg)	1.31	0.63	0.46	0.52	1.58	1.65	0.49	0.81
RTF	2.89	1.62	0.46	0.46	1.11	1.43	0.39	0.60

the lowest feature importance scores in all Fevals. Semicircular canal feedback emerges as a medium strength feature for Scenario B (Feval9 and Feval10) and only for Feval2 in Scenario A. However, the weights associated with muscle spindle function (W_{wy1}, W_{wy2}) and Golgi tendon feedback (W_{ty1}, W_{ty2}) consistently dominate in importance across almost all Fevals, except for Feval8 (RMSE of the head pitch phase in the frequency domain) which shows no importance across any feedback pathways. Furthermore, the RTF is primarily influenced by variations in W_{ty1}, W_{ty2}, $W_{w_{y1}}$, and $W_{w_{y2}}$, directly linking computational cost to the sensory feedback pathways that had the highest feature importance among Fevals. This highlights that the sensory channels most critical for matching human responses also drive computational effort, reflecting the direct trade-off between model accuracy and real-time performance.

5.3. Case-specific optimization

The cases considered across all scenarios (A, B and C) for optimization were extracted based on the above MPC sensitivity analysis and the interest in understanding the pathways' influence on head–neck model accuracy. The cases are described below:

- Case 1: Only muscle effort (F1 and F2) and partial somatosensory feedback (F5 and F6).
- Case 2: Full pathways—muscle effort (F1 and F2), somatosensory feedback (F3 to F6), otolith feedback (F7) and semicircular canal feedback (F8).
- Case 3: Muscle effort (F1 and F2), full somatosensory feedback (F3 to F6), and semicircular canal feedback (F8).

High-level optimization for tuning the MPC weights was separately performed for all Cases (1, 2, and 3) across all scenarios (A, B, and C). The first step involved optimizing each scenario independently to understand the system thoroughly. This optimization focused on two main aspects:

1. Evaluation Functions: Analyzing the relationships between the evaluation functions used in the optimization algorithms (*multiga()*), identifying the necessary trade-offs and how these differ for each case, and determining which case minimized the evaluation functions most effectively (best overall result in terms of optimized performance).
2. Cross-Scenario Optimization: Deriving a single set of MPC weights that could ensure optimal inputs by the MPC-based postural control to the head–neck model across different perturbation scenarios, while also maintaining computational efficiency.

6. Results

This section presents the results of the high- and low-level optimizations across three scenarios: Scenario A, Scenario B, and Scenario C (multi-scenario). For each, the MPC cost function weights (Eq. (22)) are tuned using high-level optimization to fit two experimental datasets. Three configurations (Case 1, Case 2, Case 3) were used. Results are evaluated based on Pareto alternatives, TOPSIS (Technique for Order of Preference by Similarity to Ideal Solution, Pandey et al. (2023))-compromised solutions, VAFs, Fevals, and RTFs.

6.1. Scenario A: Anterior-posterior perturbation

Scenario A optimizes the response to anterior–posterior perturbations across Cases 1–3. Trade-offs between evaluation functions were assessed via Pareto fronts. Conflicting Feval pairs were identified using Kendall's Tau and hypervolume reduction (ΔH_{ij}), showing Feval2 vs. Feval5 and Feval4 vs. Feval5 as most conflicting. These align with the results in Table 3 and support the rationale for multi-scenario optimization. Fig. 3 illustrates the solutions with a Pareto dominance rank of 15 or less to highlight the identified conflicts.

TOPSIS was applied to identify best-compromised MPC weights (Fig. 4). Case 3 performed best overall, excelling in Feval2, Feval4, Feval6, and Feval8. Case 1 led in three of four head pitch metrics, including Feval5, and shared Feval7 with Case 3. Case 2 did not lead in any Feval.

Fig. 5 compares simulation outputs with experimental data. MPC weights revealed that both Case 1 and 3 prioritized the lower joint: $W_{ty1} > W_{ty2}$, $W_{w_{y1}} > W_{w_{y2}}$. Case 1 showed a ratio of ≈23, while Case 3's was ≈2.5. Case 2 favored the upper joint, especially in angular position costs, with higher values for $W_{q_{y2}}$.

To assess sensitivity to specific cost components, four additional cases were created. Case 2.1 is based on Case 2 but removes the relative angular position costs ($W_{q_{y1}}, W_{q_{y2}} = 0$). Case 2.2 removes angular position, semicircular canal, and otolith costs. Similarly, Case 3.1 is based on Case 3 but excludes relative angular position costs, while Case 3.2 removes global pitch and angular velocity costs. Though these weights had high values (Table 6), feature importance analysis (Table 4) suggested weak effects. Results confirmed this: Case 2.1 and 3.1 showed <1% AVG VAF drop, whereas 2.2 and 3.2 showed more, with Case 3.2 dropping ≈7%, indicating semicircular canal costs impact pitch accuracy. Cases 1 and 3 showed similar AVG VAFs: 77.77% and 77.83%, respectively. Case 1 led in pitch metrics; Case 3 led in position. Case 2 had the lowest AVG VAF (74.63%) but outperformed Case 1 in head position. VAF differences were: $\Delta\text{VAF}pitch \approx 6.5\%$, $\Delta\text{VAF}w_{pitch} \approx 10\%$, $\Delta\text{VAF}x \approx 2\%$, $\Delta\text{VAF}v_x \approx 13\%$.

The above suggest Case 1 provided more uniform time-domain fitting, except for $\text{VAF}v_x$, which showed the largest deviation due to high-frequency content. Frequency domain results (Feval5–Feval8) showed Case 1 led in Feval5 (pitch gain), while Case 3 led in Feval6 (position gain) and Feval8 (position phase) (Table 7). Feval7 showed negligible difference. Case 3 improved Feval6 by 6.52% and Feval8 by 8.61% while Case 1 outperformed Case 3 in Feval5 by 9.03%. Case 2 followed Case 3's weight pattern but with worse overall results.

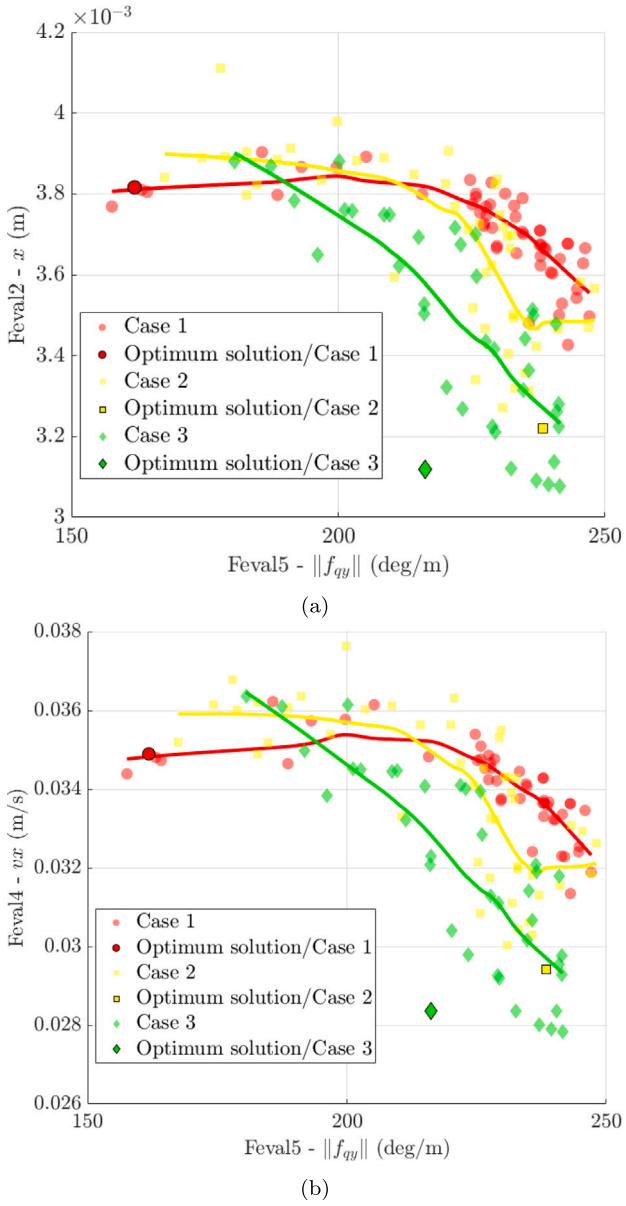

Fig. 3. Pareto dominance rank solutions (Rank ≤15) for Scenario A. Fig. 3(a): Feval2 vs. Feval5 & Fig. 3(b): Feval4 vs. Feval5.

Comparing additional cases to their bases: Cases 2.1 and 2.2 showed increased Feval5 RMSE; Feval6 worsened only for 2.2. Feval7 and Feval8 improved for Case 2.2. Similar trends appeared in Cases 3.1 and 3.2. This suggests relative angular position and otolith costs had marginal impact, indicating that most probably the high-level optimization assigned random values.

6.2. Scenario B: Pitch perturbation

Scenario B optimized pitch perturbation using Feval9 (RMSE of head pitch gain) and Feval10 (RMSE of head pitch phase). No time-domain data was available. Pareto fronts showed conflict between Feval9 and Feval10 (Fig. 6); Feval9 was prioritized. TOPSIS-selected weights showed Case 1 as the best performer in Feval9 and RTF, while Case 3 was best in Feval10.

RMSEs relative to normalized experimental ranges showed that Case 1 outperformed Case 2 by 41.88%, and Case 3 by 55.89% in Feval9 (Table 8). Case 3 outperformed Case 1 by 23.96%, and Case 2 by 7.52% in Feval10.

All cases showed $W_{w_{y1}} < W_{w_{y2}}$, especially in Case 3 (≈9). Muscle effort ratios were ≈5.25 for Case 1 and 2, indicating prioritization of the upper joint.

Additional case results showed that Case 2.1 offered a small Feval9 improvement but degraded Feval10, while Case 2.2 improved Feval10 with negligible change in Feval9. Case 3.1 and 3.2 showed similar but opposite trends, with Case 3.2 showing the largest increase in Feval10 RMSE (≈30%), highlighting the importance of semicircular canal costs.

The frequency-domain responses for Cases 1, 2, and 3, obtained using the optimal MPC weights, are compared to experimental data in Fig. 7. Overall in Scenario B, Case 1 remains the optimal case, demonstrating superior performance when additional sensory pathways are excluded from high-level optimization of the MPC weights.

6.3. Scenario C: Multi-scenario optimization

Scenario C optimized across both perturbation types using Case 1 (selected based on prior results in Scenarios A and B). Pareto fronts for Feval2 vs. Feval5 (Fig. 9(a)) and Feval4 vs. Feval5 (Fig. 9(b)) showed steeper slopes than in Scenario A. In pitch metrics, Scenario C resembled B (Fig. 8). Asymptotic behavior appeared at slope extremes, confirming the need for compromise.

TOPSIS selected weights that dominated five of ten Fevals: Feval2, Feval4, Feval6, Feval8 (anterior–posterior), and Feval10 (pitch) (Fig. 10). The weight set aligned more with Scenario B - Case 1, emphasizing upper joint torque and velocity costs (Table 5).

The AVG VAF for Scenario C was 71.02%, similar to Scenario A - Case 2.2, reflecting similar cost weight ratios. Scenario C - Case 1 achieved the second-best Feval9 and improved Feval10 (Table 9) compared to Scenario B - Case 1. Time and frequency responses are shown in Figs. 11 and 12.

7. Discussion

This study examined three distinct cases to evaluate the effects of different sensory feedback pathways and muscle effort on the head–neck system's response to perturbations. The results offer critical insights into the performance and computational efficiency of each case under anterior–posterior and pitch perturbations. Additionally, the study examined whether a single set of MPC weights could effectively stabilize the system across these varied conditions.

7.1. Scenario A: Anterior-posterior perturbations

During anterior–posterior perturbations, the almost complete (without the otolith feedback) feedback pathways demonstrated superior overall performance across evaluation functions, particularly in position-related metrics as highlighted by the optimal solutions (TOPSIS results, Fig. 4 & Table 7). Muscle effort with partial somatosensory feedback, however, provided higher accuracy in pitch-related metrics, indicating its stronger performance in pitch, angular velocity and pitch gain compared to having the complete sensory feedback without the otolith feedback. Despite the differences in the individual metrics (Fevals), the average behavior (VAFs) of both cases (complete sensory feedback without the otolith feedback, and muscle effort with partial somatosensory feedback) were nearly identical (Table 6), indicating comparable overall accuracy in the time domain. However, the individual VAF components revealed trade-offs: muscle effort and partial somatosensory feedback provided a more uniform match across three of the four VAF metrics, while complete sensory feedback without the otolith feedback exhibited a clear bias toward fitting position-related metrics. This trade-off is evident in Fig. 5(c), where the pitch gain for complete sensory feedback without the otolith feedback drops above

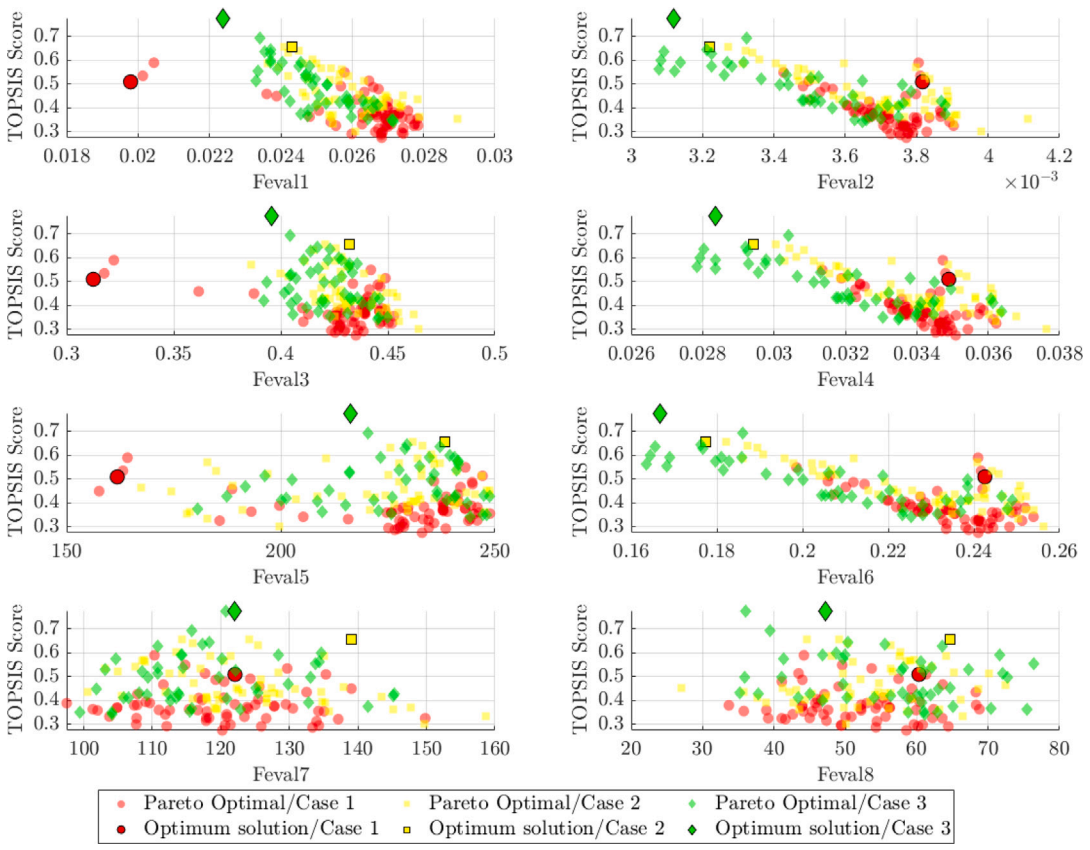

Fig. 4. TOPSIS Scores vs. Fevals in Scenario A for Case 1 (muscle+somato), Case 2 (muscle+somato+semi+oto) and Case 3 (muscle+somato+semi). Optimum solutions per Feval as derived by TOPSIS are shown as: red dot - Case 1; yellow square - Case 2 & green rhombus - Case 3.

Table 5
Optimized MPC weights across Scenarios A, B, and C for Case 1 (muscle+somato), Case 2 (muscle+somato+semi+oto), Case 3 (muscle+somato+semi), and sub-cases: Case 2.1 (Case 2 with $W_{q_{y1}}$, $W_{q_{y2}} = 0$), Case 2.2 (Case 2 with $W_{q_{y1}}$, $W_{q_{y2}}$, $W_{q_{yglob}}$, $W_{w_{yglob}} = 0$), Case 3.1 (Case 3 with $W_{q_{y1}}$, $W_{q_{y2}} = 0$) and Case 3.2 (Case 3 with $W_{q_{y1}}$, $W_{q_{y2}}$, $W_{w_{yglob}} = 0$). Dashes (—) indicate deactivated weights. RTF = Real-Time Factor.

Sc.	Case	W_{ty1}	W_{ty2}	$W_{q_{y1}}$	$W_{q_{y2}}$	$W_{w_{y1}}$	$W_{w_{y2}}$	$W_{q_{yglob}}$	$W_{w_{yglob}}$	RTF
	1	76.96	3.37	–	–	8.26	1.62	–	–	6.78
	2	18.42	70.47	65.05	87.55	46.39	68.65	70.47	84.36	7.16
	3	62.63	25.51	77.23	90.44	88.76	18.06	–	63.32	8.10
A	2.1	”	”	–	–	”	”	”	”	9.16
	2.2	”	”	–	–	”	”	–	–	10.05
	3.1	”	”	–	–	”	”	–	”	8.56
	3.2	”	”	–	–	”	”	–	–	9.72
	1	15.83	75.64	–	–	28.20	74.14	–	–	8.14
	2	11.04	63.60	23.61	67.52	19.88	32.06	19.06	7.71	9.18
	3	76.09	64.48	27.34	86.01	9.37	81.96	–	92.51	8.98
B	2.1	”	”	–	–	”	”	”	”	9.08
	2.2	”	”	–	–	”	”	–	–	10.45
	3.1	”	”	–	–	”	”	–	”	9.38
	3.2	”	”	–	–	”	”	–	–	9.95
C	1	38.09	91.56	–	–	73.00	98.45	–	–	NA

1.125 Hz, indicating a shift toward head-in-space stabilization (reduced global pitch magnitude) rather than head-on-trunk stabilization. This outcome is expected when including semi-circular canal and otolith costs, as these components penalize global head motion.

The analysis of MPC weights further clarifies these trade-offs. Both cases (complete sensory feedback without the otolith feedback, and muscle effort with partial somatosensory feedback) prioritized lower neck joint cost components. However, the significantly larger ratio between the two joint cost components (approximately 2.5 for complete sensory feedback, and approximately 23 for muscle effort with partial somatosensory feedback) emphasizes the focus of the latter on lower neck joint muscle effort. This likely contributed to superior performance in pitch metrics in the simplified feedback case, whereas the complete feedback offered more balanced prioritization of neck joint costs which supports its dominance in position-related metrics.

The additional cases showed that the angular position costs had negligible effects on model performance, suggesting that the high-level optimization process randomly assigned weights to these components. This validated the results of the weights feature importance for the developed MPC-based postural control strategy. In contrast, the removal of otolith and semi-circular canal costs significantly impacted performance. Nonetheless, muscle effort and partial somatosensory feedback

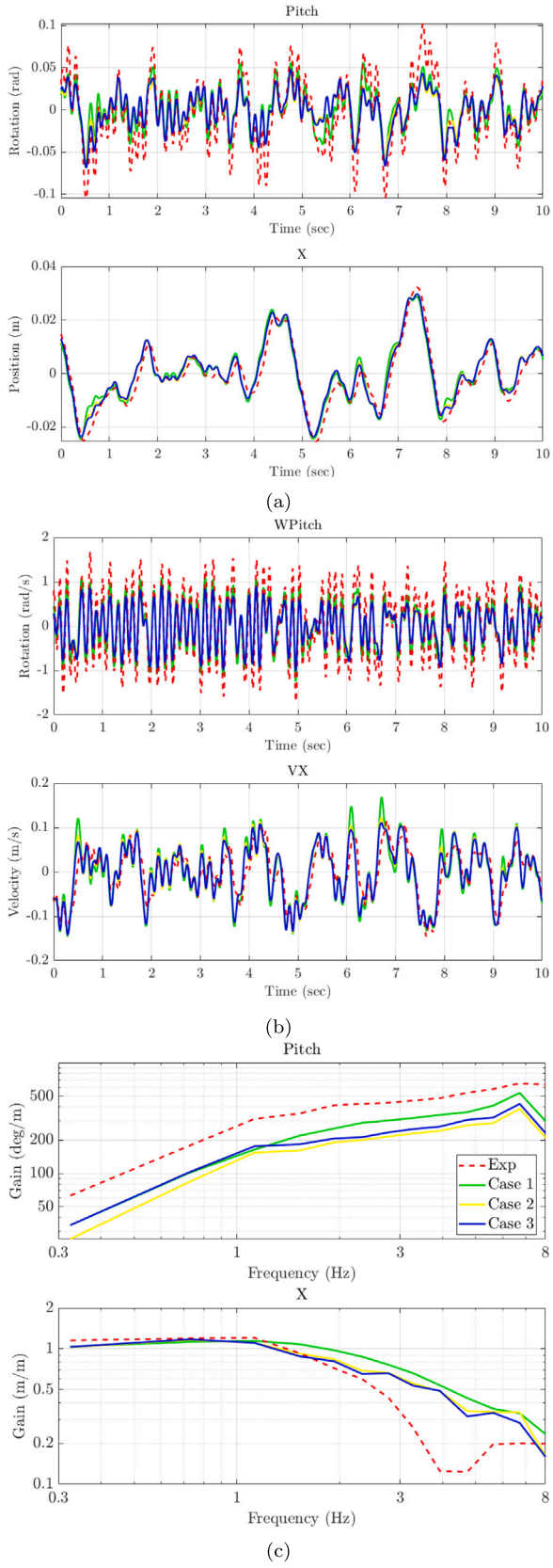

Fig. 5. Scenario A time and frequency domain experimental and simulated responses: Case 1 (muscle+somato), Case 2 (muscle+somato+semi+oto) and Case 3 (muscle+somato+semi). $N = 20$ and $T_{sim} = 0.8$ ms.

Table 6
VAFs (%) across Scenarios A and C. Time-domain metrics only; Scenario B is not applicable (NA).

Case	VAFs				
	pitch	*x*	w_{pitch}	v_x	AVG
Scenario A:					
1	76.62	89.35	83.72	61.38	77.77
2	64.69	92.42	68.85	72.55	74.63
3	70.09	92.89	73.86	74.48	77.83
2.1	63.63	92.20	68.39	71.70	73.98
2.2	59.42	91.33	66.76	68.35	71.47
3.1	69.61	92.78	73.66	74.05	77.53
3.2	58.82	89.49	71.96	61.34	70.40
Scenario C:					
1	58.61	91.05	67.00	67.44	71.02
Scenario B:					
NA					

Table 7
Fevals for Scenario A – Anterior–Posterior Perturbation. All values are RMSEs. Units: Feval1, Feval3 in rad; Feval2, Feval4 in m; Feval5 in deg/m; Feval6 in m/m; Feval7–Feval8 in deg.

Case	Fevals							
	1	2	3	4	5	6	7	8
1	0.020	3.82e−3	0.31	3.49e−2	161.81	0.24	122.06	60.31
2	0.024	3.22e−3	0.43	2.94e−2	238.39	0.18	139.07	64.61
3	0.022	3.12e−3	0.40	2.84e−2	216.24	0.17	122.01	47.21
2.1	0.025	3.27e−3	0.44	2.99e−2	240.21	0.18	118.00	45.54
2.2	0.026	3.44e−3	0.45	3.16e−2	245.83	0.20	118.75	47.74
3.1	0.023	3.14e−3	0.40	2.86e−2	217.21	0.17	151.58	68.62
3.2	0.026	3.80e−3	0.41	3.49e−2	212.34	0.24	128.37	51.45

Table 8
Fevals for Scenario B – Pitch Perturbation. Units: Feval9 in deg/deg, Feval10 in deg.

Case	Fevals	
	9	10
1	0.42	34.51
2	0.60	29.13
3	0.66	26.67
2.1	0.62	33.35
2.2	0.72	29.36
3.1	0.73	26.81
3.2	0.83	37.91

Table 9
Fevals for Scenario C – Multi-scenario optimization. Units consistent with Tables 7 and 8.

Case	Fevals									
	1	2	3	4	5	6	7	8	9	10
1	0.026	3.50e−3	0.44	3.20e−2	244.80	0.21	106.85	60.86	0.58	30.14

(relative angular velocity) emerged as the primary contributors to the model's performance.

These findings suggest that for anterior–posterior perturbations under eyes-closed conditions, simpler postural control focusing on muscle effort with partial somatosensory feedback (relative angular velocity) may suffice. This aligns with prior research (Happee et al., 2023), where muscle feedback alone could adequately describe such scenarios. Similar observations were noted in vestibular loss patients subjected to low-amplitude horizontal seat translations with their trunk strapped to the seat (Keshner, 2003).

The inclusion of additional sensory feedback pathways improved performance in position-related metrics but increased computational complexity, leading to a higher RTF compared to only muscle effort with partial somatosensory feedback. Case 2, which incorporated all

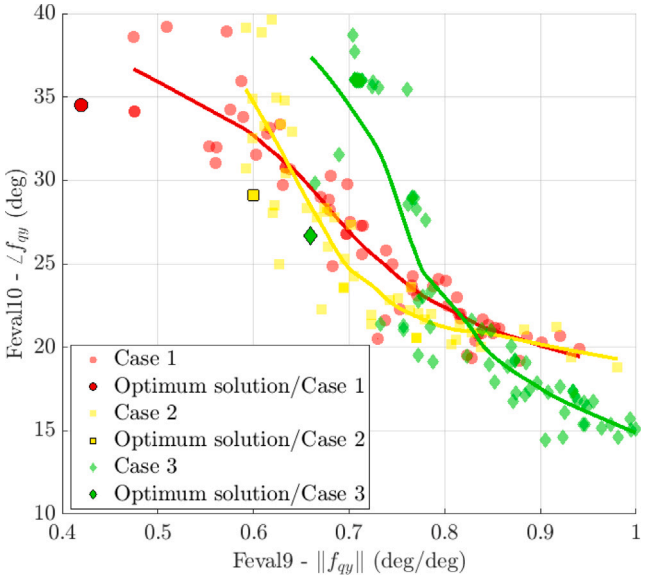

Fig. 6. Feval9 vs. Feval10 Pareto dominance rank solutions (Rank ≤15) for Case 1 (muscle+somato), Case 2 (muscle+somato+semi+oto) and Case 3 (muscle+somato+semi), in Scenario B.

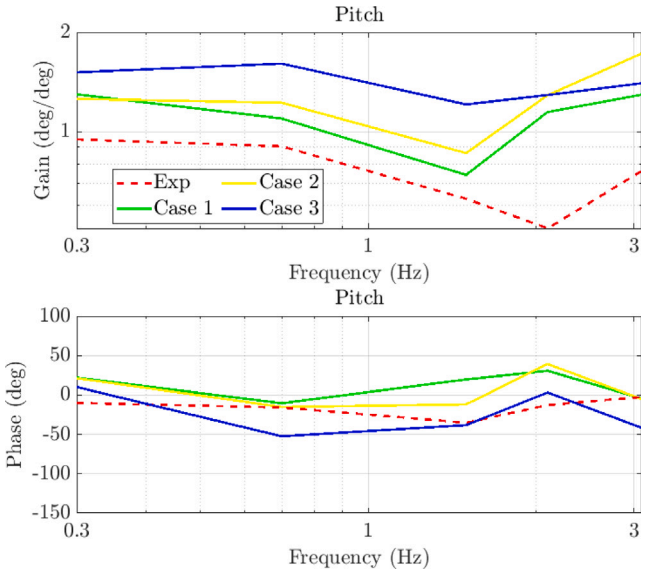

Fig. 7. Frequency domain responses for Case 1 (muscle+somato), Case 2 (muscle+somato+semi+oto) and Case 3 (muscle+somato+semi) along with experimental responses. $N = 20$ and $T_{sim} = 0.8$ ms.

sensory pathways, showed even lower performance, likely due to the more complex high level optimization introduced by the additional design variables. This additional complexity could have made the optimization complex both in terms of the MPC cost functions but also for the genetic algorithm parameter tuning in the specific scenario. However, the configuration of the genetic algorithm was selected based on default values suggested by MATLAB for the specific number of design variables.

Computationally, muscle effort with partial somatosensory feedback was the most efficient, achieving the lowest RTF of 6.78 (Table 5). For context, Happee et al. (2023) reported an RTF of approximately 100. The strong performance and efficiency of Case 1 reinforce the value of simpler biomechanical head–neck models combined with advanced postural control algorithms for this type of perturbation.

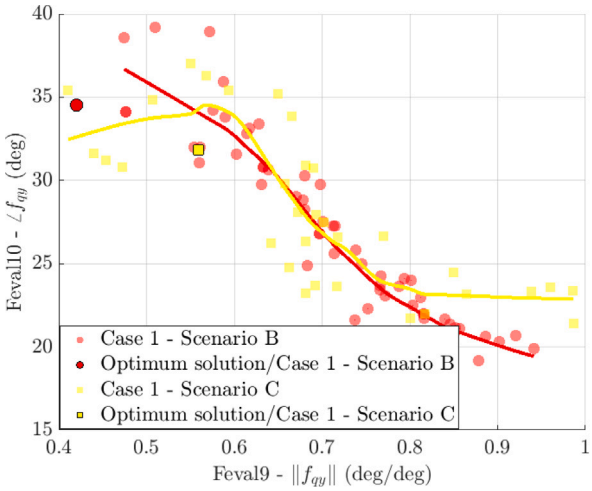

Fig. 8. Feval9 vs. Feval10 Pareto dominance rank solutions (Rank ≤15) for Case 1 in Scenario B, and Case 1 in Scenario C.

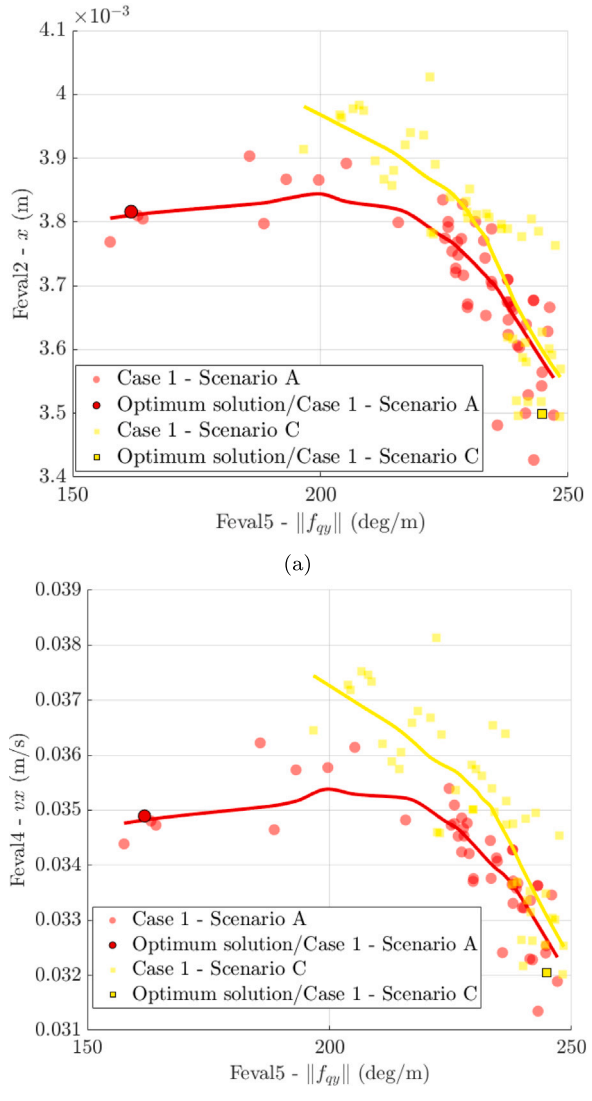

Fig. 9. (a) Feval2 vs. Feval5. (b) Feval4 vs. Feval5. Both (a) and (b) show Pareto dominance rank solutions (Rank ≤15) for Case 1 in Scenario A, and Case 1 in Scenario C.

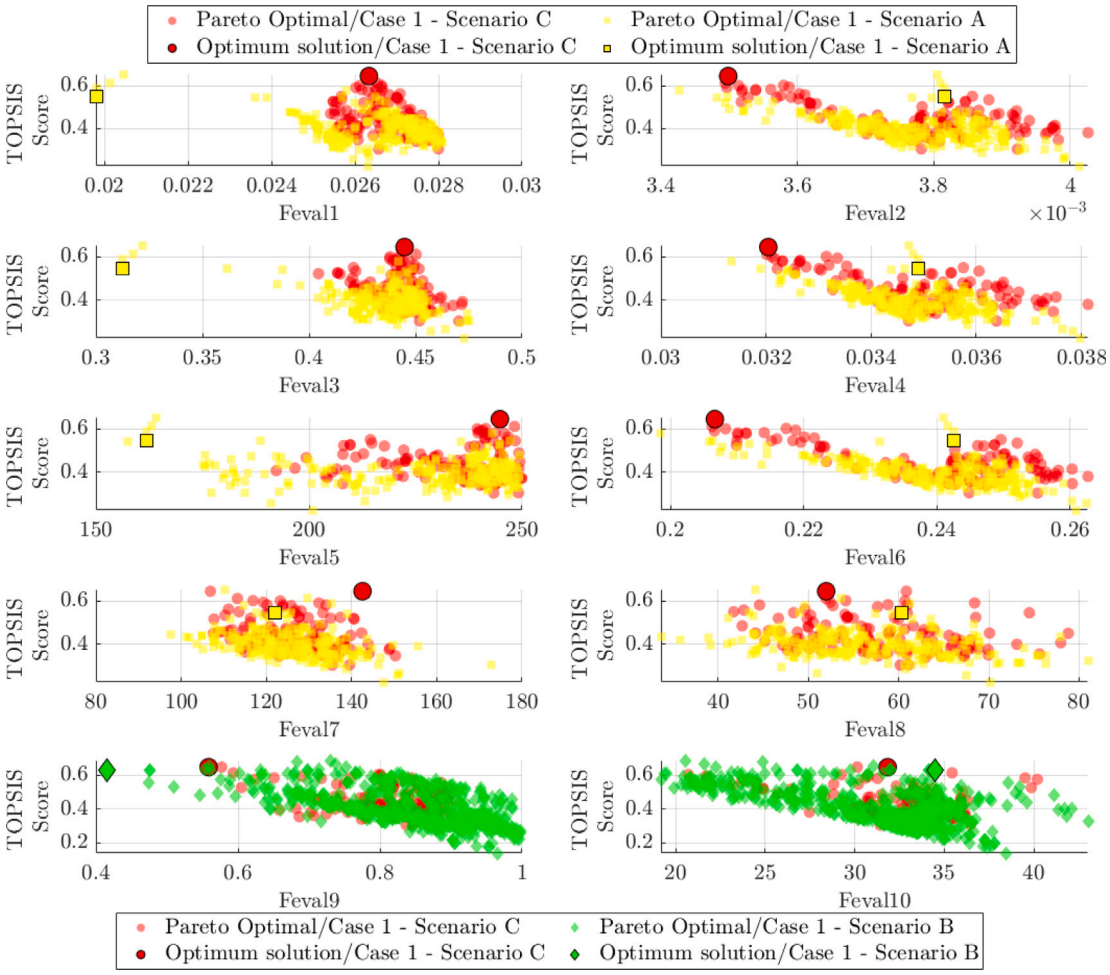

Fig. 10. TOPSIS scores vs. Fevals. Scenario C is compared with Scenario A for Feval1 - Feval8, annotating the optimum solutions (red dot - Scenario C & yellow square - Scenario A). Additionally, Scenario C is compared with Scenario B for Feval9 & Feval10, annotating the optimum solutions (red dot - Scenario C & green rhombus - Scenario B).

7.2. Scenario B: Pitch perturbations

In Scenario B, based on prior studies (Happee et al., 2023), it was anticipated that muscle effort alone would be insufficient for stabilizing the head and that semi-circular canal feedback would be critical for accurate performance. Contrary to these expectations, muscle effort and partial somatosensory feedback achieved the best overall balance across evaluation functions.

However, even the best-performing solution in Scenario B (muscle effort with partial feedback) exhibited discrepancies in low-frequency dynamics. Specifically, at 0.3 Hz and 0.7 Hz, the experimental pitch gains were below 1 (0.9487 and 0.9040, respectively), while the simulated gains exceeded 1 (1.2987 and 1.0977). This discrepancy indicates a limitation of the current MPC-based postural control in accurately capturing low-frequency behaviors when the model is excited under pitch perturbations. The reason behind this issue might be related to the current optimization method which uses as a criterion the RMSE of the experimental and simulated gain between the equally weighted 5 frequency points. Furthermore, the limited experimental data points (5 frequency points in gain and phase) and the age of the data (collected in 1995) posed additional challenges for achieving better fits during optimization.

The additional in the other cases, which represent semi-circular canal and otolith costs, did not substantially improve performance. These results suggest that in the simplified MPC-base postural control, the additional semi-circular canal feedback may have been partially redundant, given that the relative angular (or joint) velocity feedback already captured most of the critical dynamics (Eq. (22)). The addition of extra optimization variables in these cases may have complicated the optimization problem, hampering the convergence. As with the anterior–posterior perturbation, muscle effort combined with partial somatosensory feedback was also the most computationally efficient, further emphasizing the benefits of a streamlined approach.

7.3. Scenario C: Multi-scenario optimization

This scenario explored whether a single set of MPC weights could properly fit the head–neck model's response to the data across both anterior–posterior and pitch perturbations. Building on the results of the single perturbation scenario, muscle effort and partial somatosensory feedback was selected for this multi-scenario optimization.

The results indicate that the multi-scenario optimization successfully balanced the performance for both perturbation types, though trade-offs were observed. Interestingly, the optimal weights for the multi-scenario aligned more closely with the pitch perturbations than the anterior–posterior perturbations. The weights prioritized upper neck joint components, mirroring the trend observed in pitch perturbations. This suggests that incorporating pitch perturbations in the optimization process shifted the emphasis toward upper neck dynamics. The average VAF for Scenario C was closely resembling the performance of the case where semi-circular canal, otolith, and relative position costs were deactivated (Case 2.2). This similarity indicates that the additional Fevals for pitch gain and phase in the high-level optimization for tuning, introduced a cost penalty on global head

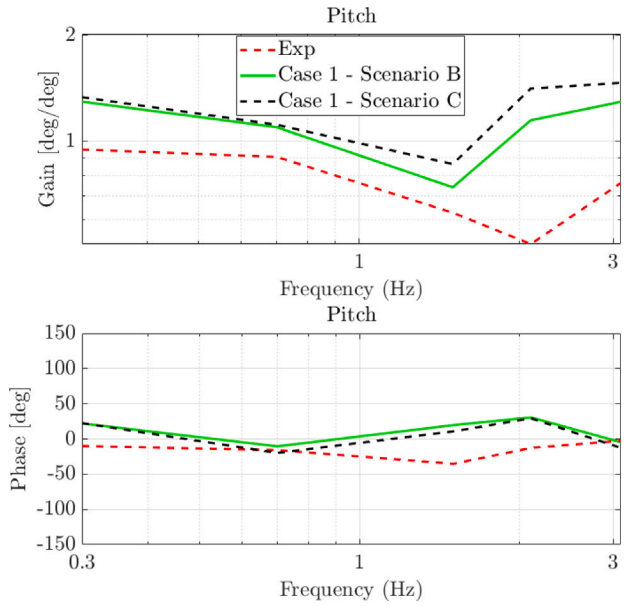

Fig. 11. Response for multi-scenario optimization in pitch perturbation comparing Case 1 in Scenario B, Case 1 in Scenario C, and experimental data, in the frequency domain. $N = 20$ and $T_{sim} = 0.8$ ms.

pitch motion, favoring head-in-space stabilization. This trend is also evident in Fig. 7, where the experimental gain is below 1, reflecting a head-in-space control strategy.

In this scenario, the muscle effort with partial somatosensory feedback achieved the second-best fitting for head pitch gain for pitch perturbations. However, a notable imbalance in the optimization process favored anterior–posterior metrics due to the disproportionate number of Fevals (5 for anterior–posterior vs. 2 for pitch perturbations). This bias could suggest that achieving a truly balanced multi-scenario solution would require equal representation of evaluation functions for both perturbation types.

The AVG VAF reflects a reduction in overall accuracy compared to single-scenario setups. Future refinements could include adaptive weights or frequency-dependent optimizations to address these trade-offs. Studies on alert macaques (Carriot et al., 2015) have shown that the integration of rotational (semi-circular canal) and translational (otolith) inputs is frequency-dependent, with canals dominating at lower frequencies and otoliths becoming more significant at higher frequencies. Incorporating such frequency-dependent adjustments into the MPC framework could improve performance under multi-dimensional perturbations.

7.4. Limitations

While the MPC-based postural control offers a novel approach to modeling compensatory postural control in the head–neck system, there are limitations that merit further exploration.

The MPC algorithm is limited by its reliance on predefined models and static optimization horizons. This makes it less adaptive in scenarios requiring real-time learning and adjustment, as might be expected in a biologically plausible representation of the CNS. The CNS's postural control mechanisms are thought to adapt and learn from repeated exposures to perturbations, a feature not yet captured in the current MPC framework. Furthermore, the model should be adaptive to different postures and initial conditions, because variations in starting postures affect the entire dynamic response.

The model currently assumes perfect sensory perception, excluding the influence of sensory delays and noise. The CNS, however, operates

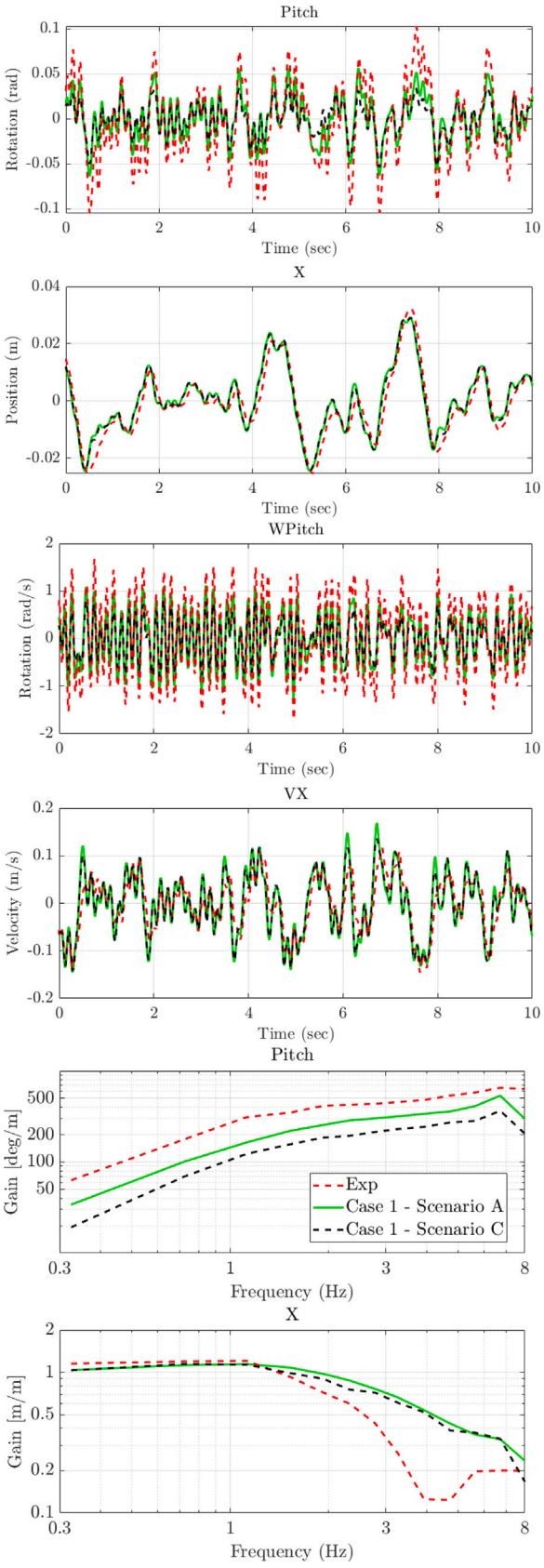

Fig. 12. Response for multi-scenario optimization in anterior–posterior perturbation comparing Case 1 in Scenario A, Case 1 in Scenario C, and experimental data, in the time and frequency domain. $N = 20$ and $T_{sim} = 0.8$ ms.

under conditions of incomplete and noisy sensory feedback, necessitating robust strategies to integrate delayed or uncertain information. While this simplification enhances computational efficiency, it limits the realism of the model, particularly under conditions involving rapid or complex perturbations.

The parameter tuning of the model was considered during unexpected events (i.e., compensatory postural control without anticipation) excluding visual feedback. These scenarios are more relevant for automated vehicles or trains where occupants engage in non-driving related tasks and are not able to anticipate upcoming motion. However, further work is required to explore the ability of the model to capture accurately the response of the head–neck system during perturbation where occupants anticipate the upcoming motion (i.e., activation of anticipatory postural adjustments). Another aspect is that the model was only tested in perturbations in sagittal plane. Hence, it has to be validated in more dynamic driving scenarios where six dimensional perturbations are provided.

8. Conclusions

This study presented a novel MPC-based framework to simulate CNS-inspired head–neck postural stabilization strategies under dynamic perturbations. The first key contribution is the development of an MPC-based postural control algorithm that integrates the fundamental behavior of the CNS, including the neural store, sensory integration, and minimization of sensory conflict as a guiding principle for motor control. This approach balances computational efficiency and modeling accuracy, addressing limitations in existing methods.

The second contribution is a detailed evaluation of sensory pathways – muscle effort, somatosensory input, semicircular canals, and otolith organs – and their effects on stabilization accuracy and computational load. The findings demonstrate that muscle effort and partial somatosensory feedback are sufficient for predicting accurate stabilization, minimizing computational demand. While additional vestibular feedback pathways offered marginal benefits in accuracy, they increased computational complexity, emphasizing the trade-offs involved in sensory pathway inclusion in eyes closed conditions.

The third contribution is the demonstration that a single set of MPC weights can effectively generalize well across anterior–posterior and pitch perturbations, suggesting the potential for unified control strategies in dynamic environments.

Overall, the framework provides a computationally efficient, biologically plausible alternative to complex multi-segment models and enhances the understanding of CNS-inspired postural control. Beyond fundamental research, it could be integrated into vehicle control modules or design processes to improve motion comfort. The predicted dynamic responses may also support motion sickness and comfort assessment models. Further work is ongoing to address current limitations and extend the model to more diverse motion scenarios.

CRediT authorship contribution statement

Chrysovalanto Messiou: Writing – original draft, Visualization, Validation, Software, Methodology, Formal analysis, Conceptualization. **Riender Happee:** Writing – review & editing, Supervision, Software, Resources, Project administration, Funding acquisition. **Georgios Papaioannou:** Writing – review & editing, Supervision, Resources, Project administration, Funding acquisition, Conceptualization.

Declaration of competing interest

The authors declare that they have no known competing financial interests or personal relationships that could have appeared to influence the work reported in this paper.

Appendix A. FORCESPRO solver options

Solver options	Value	Description
`codeoptions.maxit`	200	QP solver uses no more than 200 iterations to solve a problem
`codeoptions.optlevel`	3	0: no optimization, 1: optimize for size, 2: optimize for speed, 3: optimize for size & speed
`codeoptions.nlp.integrator.type`	'ERK4'	Integrator functions
`codeoptions.nlp.integrator.Ts`	$1e{-}2$	Absolute time between two integration intervals (T_{sp})
`codeoptions.nlp.integrator.nodes`	1	Defines the number of intermediate nodes
`codeoptions.solvemethod`	'PDIP_NLP'	Set optimization method
`codeoptions.BuildSimulinkBlock`	1	Simulink block is compiled
`codeoptions.parallel`	1	Internal parallelization of the solver using OpenMP
`codeoptions.threadSafeStorage`	1	Generated solver is thread safe
`codeoptions.nlp.TolStat`	$1e{-}1$	Infinity norm tolerance on stationarity
`codeoptions.nlp.TolEq`	$1e{-}3$	Tolerance on equality constraints
`codeoptions.nlp.TolComp`	$1e{-}1$	Tolerance on complementarity
`codeoptions.accuracy.eq`	$1e{-}3$	Infinity norm of residual for equalities
`codeoptions.accuracy.mu`	$1e{-}6$	Absolute duality gap
`codeoptions.accuracy.rdgap`	$1e{-}2$	Relative duality $gap := (pobj - dobj)/pobj$
`codeoptions.nohash`	1	Enforce solver regeneration
`codeoptions.overwrite`	1	Overwrite existing solver
`codeoptions.nlp.ad_expression_class`	'MX'	Automatic differentiation expression class

Appendix B. Simulation timestep and prediction horizon

Various combinations of N and T_{sp} were tested for Scenario A, with N ranging from 20 to 45 to 20. According to the results, a T_H of less than 200 ms led to unstable responses, emphasizing the importance of maintaining an appropriate prediction window. Table B.10 outlines all the tested parameters. Fig. B.13(a) illustrates the relationship between N and Average VAFs, with each data point labeled according to its T_H. Fig. B.13(b) displays the relationship between N and RTF, showing that

Table B.10
Examined range of prediction forecast, horizon, and timestep.

	Values					
Forecast horizon (T_H [ms])	225	200	245	210	225	200
Prediction horizon (N)	45	40	35	30	25	20
Prediction timestep (T_{sp} [ms])	5	5	7	7	9	10

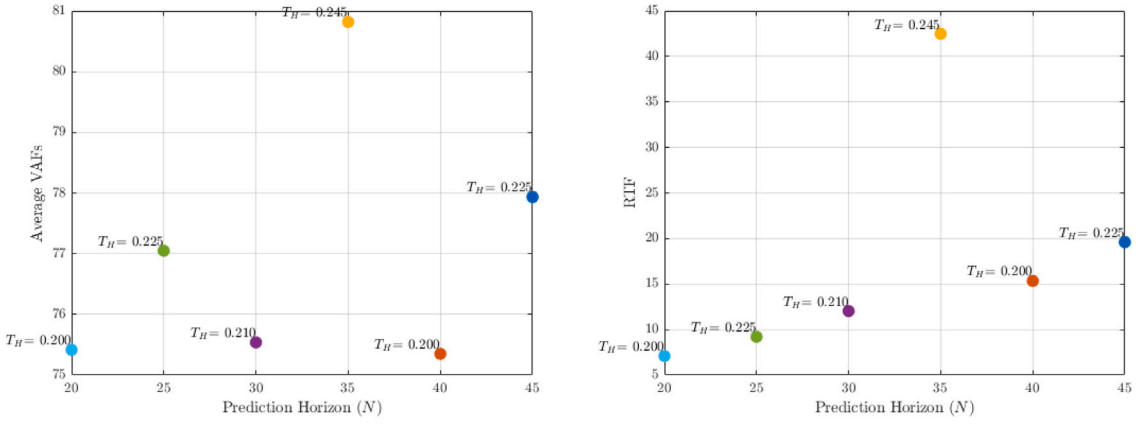

(a) (b)

Fig. B.13. The left plot shows the average VAFs vs. N, while the right plot presents the RTF vs. N. Labels show the respective T_H in seconds.

Table B.11
Simulation timestep, RTF, and VAF Values.

T_{sim}	RTF	VAF_Pitch (%)	VAF_X (%)	VAF_WPitch (%)	VAF_VX (%)	AVG VAF (%)
0.004	13.30	72.25	88.08	63.33	54.03	69.42
0.005	10.87	72.99	88.39	66.79	55.98	71.04
0.006	9.06	74.98	89.21	75.25	59.50	74.73
0.007	8.01	74.66	88.49	79.26	57.53	74.99
0.008	6.97	76.62	89.35	83.72	61.38	77.77
0.009	6.20	76.21	90.14	78.38	63.94	77.17
0.010	5.52	75.84	89.94	77.92	64.42	77.03

reducing N generally improves RTF, while increasing T_H enhances the average VAFs. However, it is important to note that RTF is not solely dependent on N, as evidenced by the larger RTF observed at $N = 35$, likely due to the corresponding larger T_H.

Additionally, the optimal simulation timestep T_{sim} is determined by experimenting with values starting from 4 ms and incrementing by 1 ms up to 11 ms. The response accuracy improved consistently until 8 ms; however, at 11 ms, the head–neck model response became unstable, hence VAFs for the respective T_{sim} are not included in Table B.11. This led us to conclude that a T_{sim} of 8 ms offered the best accuracy and stability. The outcomes of these tests are detailed in Table B.11, which presents the various T_{sim} values tested alongside the corresponding VAFs for head pitch (VAF_Pitch), head position (VAF_X), head angular velocity (VAF_WPitch), head linear velocity (VAF_VX), and the average VAFs (AVG VAF) for Scenario A. Hence, the optimal configuration identified was a fixed T_H of 200 ms with a fixed N equal to 20 and T_{sp} equal to 10 ms, along with a T_{sim} of 8 ms. These configurations ensured that the head–neck model performed efficiently, maintaining both accuracy and stability.

Appendix C. Supplementary data

Supplementary material related to this article can be found online at https://doi.org/10.1016/j.conengprac.2025.106428.

References

Almeida, J., Fraga, F., Silva, M., & Silva-Carvalho, L. (2009). Feedback control of the head-neck complex for nonimpact scenarios using multibody dynamics. *Multibody System Dynamics*, *21*, 395–416. http://dx.doi.org/10.1007/s11044-009-9148-4.

Bos, J., & Bles, W. (1998). *Brain Research Bulletin*, *47*(5), 537–542. http://dx.doi.org/10.1016/S0361-9230(98)00088-4, URL: https://www.sciencedirect.com/science/article/pii/S0361923098000884.

Brolin, K., Hedenstierna, S., Halldin, P., Bass, C., & Alem, N. (2008). The importance of muscle tension on the outcome of impacts with a major vertical component. *International Journal of Crashworthiness*, *13*, 487–498. http://dx.doi.org/10.1080/13588260802215510.

Carriot, J., Jamali, M., Brooks, J. X., & Cullen, K. E. (2015). Integration of canal and otolith inputs by central vestibular neurons is subadditive for both active and passive self-motion: Implication for perception. *The Journal of Neuroscience*, *35*, 3555–3565, URL: https://api.semanticscholar.org/CorpusID:33099141.

Chen, B., Lee, Y.-J., & Aruin, A. S. (2015). Anticipatory and compensatory postural adjustments in conditions of body asymmetry induced by holding an object. *Experimental Brain Research*, *233*(11), 3087–3096. http://dx.doi.org/10.1007/s00221-015-4377-7.

Cheng, H., Obergefell, L., Rizer, A., & Directorate, A. L. C. S. (1994). *Generator of body (GEBOD) manual*. (U.S.): Armstrong Laboratory, Air Force Material Command, URL: https://books.google.nl/books?id=xvuYtgAACAAJ.

Cole, D. J. (2018). Occupant–vehicle dynamics and the role of the internal model. *Vehicle System Dynamics*, *56*(5), 661–688. http://dx.doi.org/10.1080/00423114.2017.1398342.

Correia, M. A., McLachlin, S. D., & Cronin, D. S. (2020). Optimization of muscle activation schemes in a finite element neck model simulating volunteer frontal impact scenarios. *Journal of Biomechanics*, *104*, Article 109754. http://dx.doi.org/10.1016/j.jbiomech.2020.109754.

Correia, M. A., McLachlin, S. D., & Cronin, D. S. (2021). Vestibulocollic and cervicocollic muscle reflexes in a finite element neck model during multidirectional impacts. *Annals of Biomedical Engineering*, *49*, 1645–1656. http://dx.doi.org/10.1007/s10439-021-02783-2.

Fard, M. A., Ishihara, T., & Inooka, H. (2003). Dynamics of the head-neck complex in response to the trunk horizontal vibration: Modeling and identification. *Journal of Biomechanical Engineering*, *125*, 533–539. http://dx.doi.org/10.1115/1.1589777.

Fieldhouse, H., & Cole, D. (2024). *State estimation and sensorimotor noise in a driver steering model with a Gaussian process internal model* (pp. 64–70). Springer Nature Switzerland, http://dx.doi.org/10.1007/978-3-031-70392-8_10.

Forbes, P. A., De Bruijn, E., Schouten, A. C., Van Der Helm, F. C. T., & Happee, R. (2013). Dependency of human neck reflex responses on the bandwidth of pseudorandom anterior-posterior torso perturbations. *Experimental Brain Research*, *226*(1), 1–14. http://dx.doi.org/10.1007/s00221-012-3388-x, URL: https://www.scopus.com/inward/record.uri?eid=2-s2.0-84872177357&doi=10.1007%2fs00221-012-3388-x&partnerID=40&md5=b1dddc100f1219c8c0831ed03334c089.

Friston, K. (2011). What is optimal about motor control? *Neuron*, *72*(3), 488–498. http://dx.doi.org/10.1016/j.neuron.2011.10.018, URL: https://www.sciencedirect.com/science/article/pii/S0896627311009305.

Happee, R., Bruijn, E., Forbes, P. A., Drunen, P., Van Dieën, J. H., & Van Der Helm, F. C. T. (2019). Neck postural stabilization, motion comfort, and impact simulation. *DHM and Posturography*, 243–260. http://dx.doi.org/10.1016/B978-0-12-816713-7.00019-2, URL: https://www.scopus.com/inward/record.uri?eid=2-s2.0-85081322854&doi=10.1016%2fB978-0-12-816713-7.00019-2&partnerID=40&md5=4638261f35484b21df494617b0871480.

Happee, R., Kotian, V., & De Winkel, K. N. (2023). Neck stabilization through sensory integration of vestibular and visual motion cues. *Frontiers in Neurology*, *14*, http://dx.doi.org/10.3389/fneur.2023.1266345.

Hedenstierna, S., & Halldin, P. (2008). How does a three-dimensional continuum muscle model affect the kinematics and muscle strains of a finite element neck model compared to a discrete muscle model in rear-end, frontal, and lateral impacts. *Spine*, *33*, E236–245. http://dx.doi.org/10.1097/BRS.0b013e31816b8812.

International Organization for Standardization (1997). *ISO 2631-1:1997 - mechanical vibration and shock — evaluation of human exposure to whole-body vibration — part 1: general requirements*. Geneva: ISO, URL: https://www.iso.org/standard/32178.html. [Accessed 29 October 2024].

Keshner, E. A. (2003). Head-trunk coordination during linear anterior-posterior translations.. *Journal of Neurophysiology*, *89 4*, 1891–1901, URL: https://api.semanticscholar.org/CorpusID:7504977.

Keshner, E. A., Cromwell, R. L., & Peterson, B. W. (1995). Mechanisms controlling human head stabilization. II. Head-neck characteristics during random rotations in the vertical plane. *Journal of Neurophysiology*, *73*(6), 2302–2312. http://dx.doi.org/10.1152/jn.1995.73.6.2302, URL: https://journals.physiology.org/doi/abs/10.1152/jn.1995.73.6.2302.

Kyriakidis, M., Happee, R., & De Winter, J. C. F. (2015). Public opinion on automated driving: Results of an international questionnaire among 5000 respondents. *Transportation Research Part F: Traffic Psychology and Behaviour*, *32*, 127–140. http://dx.doi.org/10.1016/j.trf.2015.04.014.

Liang, H., Kaewmanee, T., & Aruin, A. S. (2020). The role of an auditory cue in generating anticipatory postural adjustments in response to an external perturbation. *Experimental Brain Research*, *238*(3), 631–641.

Lindroth, P., Patriksson, M., & Strömberg, A.-B. (2010). Approximating the Pareto optimal set using a reduced set of objective functions. *European Journal of Operational Research*, *207*(3), 1519–1534. http://dx.doi.org/10.1016/j.ejor.2010.07.004, URL: https://www.sciencedirect.com/science/article/pii/S0377221710004868.

Lo Martire, R., Gladh, K., Westman, A., & Äng, B. O. (2017). Neck muscle EMG-force relationship and its reliability during isometric contractions. *Sports Medicine - Open*, *3*(1), http://dx.doi.org/10.1186/s40798-017-0083-2.

Messiou, C., Papaioannou, G., & Happee, R. (2023). Modelling neck postural stabilization using optimal control techniques for dynamic driving. (pp. 177–185). Springer Nature Switzerland, http://dx.doi.org/10.1007/978-3-031-37848-5_20.

Meyer, F., Bourdet, N., Gunzel, K., & Willinger, R. (2013). Development and validation of a coupled head-neck FEM – application to Whiplash injury criteria investigation. *International Journal of Crashworthiness*, *18*, 40–63. http://dx.doi.org/10.1080/13588265.2012.732293.

Moriguchi, C., Carnaz, L., Alencar, J., Júnior, L., Granqvist, L., Hansson, G.-Å., & Coury, H. (2011). Postures and movements in the most common tasks of power line workers. *Industrial Health*, *49*, 482–491. http://dx.doi.org/10.2486/indhealth.MS1252.

Newman, M. C. (2009). *A multisensory observer model for human spatial orientation perception* (Ph.D. thesis), Massachusetts Institute of Technology.

Oman, C. M. (1982). A heuristic mathematical model for the dynamics of sensory conflict and motion sickness. *Acta Otolaryngologica Supplementum*, *392*, 1–44.

Oman, C. M. (1991). Sensory conflict in motion sickness: an observer theory approach. In S. R. Ellis (Ed.), *Pictorial communication in real and virtual environments* (pp. 362–376). London: Taylor & Francis.

Paddan, G. S., & Griffin, M. J. (1994). Transmission of roll and pitch seat vibration to the head. *Ergonomics*, *37*(9), 1513–1531. http://dx.doi.org/10.1080/00140139408964931.

Pandey, V., Komal, & Dincer, H. (2023). A review on TOPSIS method and its extensions for different applications with recent development. *Soft Computing*, *27*(23), 18011–18039. http://dx.doi.org/10.1007/s00500-023-09011-0.

Papaioannou, G., Desai, R., & Happee, R. (2023). The impact of body and head dynamics on motion comfort assessment. arXiv preprint arXiv:2307.03608.

Papaioannou, G., & Koulocheris, D. (2018). An approach for minimizing the number of objective functions in the optimization of vehicle suspension systems. *Journal of Sound and Vibration*, *435*, 149–169.

Papaioannou, G., Shen, C., Rothhämel, M., & Happee, R. (2025). Occupants' comfort: what about human body dynamics in road and rail vehicles? *Vehicle System Dynamics*, 1–59.

Parr, T., Pezzulo, G., & Friston, K. J. (2022). *Active inference: the free energy principle in mind, brain, and behavior*. The MIT Press, http://dx.doi.org/10.7551/mitpress/12441.001.0001.

Peng, G. C. Y., Hain, T. C., & Peterson, B. W. (1997). How is the head held up? Modeling mechanisms for head stability in the sagittal plane. *vol. 18*, In *Proceedings of the 18th annual international conference of the IEEE engineering in medicine and biology society* (pp. 1–5).

Peng, G. C., Hain, T. C., & Peterson, B. W. (1999). Predicting vestibular, proprioceptive, and biomechanical control strategies in normal and pathological head movements. *IEEE Transactions on Biomedical Engineering*, *46*, 1269–1280. http://dx.doi.org/10.1109/10.797986.

Santos, M. J., Kanekar, N., & Aruin, A. S. (2010). The role of anticipatory postural adjustments in compensatory control of posture: 1. Electromyographic analysis. *Journal of Electromyography and Kinesiology*, *20*, 388–397.

Schwab, H. V., & L., A. (2020). Multibody dynamics, TMT method. In *Advanced dynamics* (3rd ed.). Delft University of Technology.

Stemper, B. D., Yoganandan, N., & Pintar, F. A. (2004). Validation of a head-neck computer model for whiplash simulation. *Medical & Biological Engineering & Computing*, *42*, 333–338. http://dx.doi.org/10.1007/BF02344708.

Tierney, G., Gildea, K., Krosshaug, T., & Simms, C. (2019). Analysis of ball carrier head motion during a rugby union tackle without direct head contact: A case study. *International Journal of Sports Science & Coaching*, *14*, Article 174795411983347. http://dx.doi.org/10.1177/1747954119833477.

Van Ee, C. A., Nightingale, R. W., Camacho, D. L., Chancey, V. C., Knaub, K. E., Sun, E. A., et al. (2000). Tensile properties of the human muscular and ligamentous cervical spine. *Stapp Car Crash Journal*, *44*, 85–102.

Wada, T. (2021). Computational model of motion sickness describing the effects of learning exogenous motion dynamics. *Frontiers in Systems Neuroscience*, *15*, http://dx.doi.org/10.3389/fnsys.2021.634604, URL: https://www.frontiersin.org/articles/10.3389/fnsys.2021.634604.

Zanelli, A., Domahidi, A., Jerez, J., & Morari, M. (2017). FORCES NLP: an efficient implementation of interior-point... methods for multistage nonlinear nonconvex programs. *International Journal of Control*, 1–17.